nature metabolism

Article

https://doi.org/10.1038/s42255-025-01413-8

Inhibition of IRAK4 by microbial trimethylamine blunts metabolic inflammation and ameliorates glycemic control

Received: 22 May 2024

Accepted: 22 October 2025

Published online: 8 December 2025

Check for updates

A list of authors and their affiliations appears at the end of the paper

The global type 2 diabetes epidemic is a major health crisis. Although the microbiome has roles in the onset of insulin resistance (IR), low-grade inflammation and diabetes, the microbial compounds controlling these processes remain to be discovered. Here, we show that the microbial metabolite trimethylamine (TMA) decouples inflammation and IR from diet-induced obesity by inhibiting interleukin-1 receptor-associated kinase 4 (IRAK4), a central kinase in the Toll-like receptor pathway sensing danger signals. TMA blunts TLR4 signalling in primary human hepatocytes and peripheral blood monocytic cells and rescues mouse survival after lipopolysaccharide-induced septic shock. Genetic deletion and chemical inhibition of IRAK4 result in metabolic and immune improvements in high-fat diets. Remarkably, our results suggest that TMA—unlike its liver co-metabolite trimethylamine *N*-oxide, which is associated with cardiovascular disease—improves immune tone and glycemic control in diet-induced obesity. Altogether, this study supports the emerging role of the kinome in the microbial–mammalian chemical crosstalk.

Globally, diabetes affects 529 million individuals[1], claiming 1.6 million lives per year according to the World Health Organization. IR is a multifactorial condition and is now increasingly common owing to, among other factors, the increase in prevalence of a sedentary lifestyle, Western-style foods and obesity. IR is a risk factor for developing type 2 diabetes and cardiovascular diseases[2]. One of the hallmarks of these disorders is the early development of chronic, systemic, low-grade inflammation[3]. The interaction between a high-fat diet (HFD) and the gut microbiome has a strong impact on the onset of IR[4–6]: bacterial lipopolysaccharides (LPS) and dietary fats trigger low-grade inflammation[2] through activation of Toll-like receptor 4 (TLR4), a process called metabolic endotoxemia[7].

This process is supported by complex communication that occurs between the gut microbiota and the innate immune system[8], with consequences on metabolic homoeostasis[9]. Although some of the functional signalling molecules mediating microbial–mammalian chemical crosstalk have been characterized, a limited number of metabolite classes and their targets have been identified (G-protein-coupled[10] and nuclear receptors[11]). However, it has been hypothesized that microbial metabolites potentially affect other pharmacological target classes, such as kinases[12]. In previous studies, we and others have identified a family of microbiome-associated metabolites, methylamines, associated with IR, non-alcoholic fatty liver disease[13] and atherosclerosis[14], but their mechanisms of action on mammalian hosts remain unclear.

TMA is one of the most abundant microbial metabolites produced by the gut microbiota. Previously, we reported that TMA may be associated with IR[12]. TMA results from microbial metabolism of dietary choline, carnitine and trimethylamine *N*-oxide (TMAO)[15–19] before being absorbed and *N*-oxidized into TMAO by hepatic flavin-containing mono-oxygenase 3 (FMO3)[20]. After initial reports associating TMAO with adverse cardiovascular outcomes[13,16], it has since emerged that

e-mail: m.dumas@imperial.ac.uk

FMO3 inactivation was beneficial for several metabolic outcomes[21–24], strongly suggesting that TMA and TMAO have distinct biological roles.

Here, we decipher the role of TMA in the microbiota–host kinome chemical crosstalk in IR through (1) identification of gut-derived microbial metabolites associated with HFD-induced impaired glucose tolerance (IGT), IR and obesity; (2) pharmacological target screening of discriminant microbial metabolites; and (3) mechanistic validation of the pathophysiological relevance of pharmacological interactions with in vitro and in vivo models. Using this approach, we discovered a mechanism by which gut microbial TMA acts as an IRAK4 inhibitor and directly improves the host immune and metabolic tone.

Lack of hepatic inflammation in HFD and the choline supplementation hypothesis

We initially carried out longitudinal pathophysiological monitoring in a cohort of C57BL/6J mice (n = 5 for HFD and n = 6 for chow diet (CHD)), which rapidly developed obesity and IGT when fed a 65% kCal HFD with a range of macronutrient and micronutrient differences compared to CHD (Extended Data Fig. 1a,b, Fig. 1a and Supplementary Table 1). Liver transcriptomics (n = 5–6 per diet group) identified 2,084 significantly (false discovery rate of <0.1) differentially expressed genes between CHD-fed and HFD-fed mice (Extended Data Fig. 1c, Fig. 1b and Supplementary Table 1). Gene ontology and signalling pathway impact analyses (Extended Data Fig. 2 and Supplementary Tables 2–4) demonstrated upregulation of protein processing in the endoplasmic reticulum, whereas carbohydrate metabolism, circadian rhythm and AMPK signalling were significantly inhibited, consistent with existing literature[25,26]. Surprisingly, inflammation-associated pathways were not differentially affected: expression of genes coding for acute-phase serum amyloid A proteins, *Saa1* and *Saa2*, which are upregulated in response to acute inflammation and associated with type 2 diabetes, was reduced, whereas expression of pro-inflammatory cytokines such as *Il6* and *Il1β* was not significant (Fig. 1b and Supplementary Table 4). This is in contrast to established knowledge, as low-grade inflammation is one of the key features associated with IR[2,6] and HFD[27]. In addition to the percentage of fat content as a macronutrient, we therefore looked for variation in micronutrients and microbial metabolites that may contribute to this phenotype by performing metabolic profiling of the urinary metabolome of this mouse cohort (CHD and HFD, four time-points) by proton nuclear magnetic resonance (^{1}H-NMR) spectroscopy, followed by multivariate modelling. Our analysis showed that diet is the main factor influencing the metabolic profiles, followed by age (Extended Data Fig. 1d), with the model's goodness-of-prediction parameters being highly significant upon permutation testing (Extended Data Fig. 1e). The urinary metabolic signature of HFD feeding compared to CHD was mainly associated with TMA excretion (Fig. 1c), consistent with our previous reports using this diet[13,28]. We used variance components analysis to decompose the contribution of diet and age to the excretion of these three metabolites, showing that the HFD contribution overwhelms the contribution of age (Fig. 1d). Given that the HFD contains >15 g of choline per kg of diet, we then investigated whether supplementation of this micronutrient could modulate the metabolic and immune variation in response to HFD feeding.

Choline supplementation corrects HFD-induced inflammation and IR

To test the effect of choline supplementation itself on glucose tolerance and IR in an HFD context, we initiated a series of in vivo studies. We first fed C57BL/6J mice with a 65% kCal HFD containing 2 g kg^{-1} or 17 g kg^{-1} of choline (that is, LC-HFD and HC-HFD, respectively; Fig. 1e–n). To evaluate metabolic homoeostasis, we performed glucose tolerance tests (GTTs), which displayed a similar pattern with normalization of cumulative glycemia on HC-HFD compared to LC-HFD (Fig. 1e,f). Body weight was significantly increased in mice fed a LC-HFD from weaning until 5 months of age compared to mice fed a CHD and, remarkably, compared to mice fed HC-HFD (Fig. 1g), which was not related to food intake (Extended Data Fig. 3a). We then profiled circulating pro-inflammatory cytokines such as IL-6, IL-1β and TNF (Fig. 1h–j) and phosphorylation of NF-κB regulating their transcription (Extended Data Fig. 3b,c), which was also suggestive of an improvement of HFD-induced inflammation by choline supplementation.

Targeted analysis of choline and methylamine pathways

To document the effect of choline supplementation on choline-related metabolic pathways, we further refined our isotopic quantification using ultra-performance liquid chromatography with tandem mass spectrometry (UPLC–MS/MS)[29,30] to evaluate plasma concentrations of choline-derived and carnitine-derived metabolites leading to TMA and TMAO (Extended Data Fig. 3d,e). An orthogonal partial least squares discriminant analysis (O-PLS-DA) model significantly segregates the three treatment groups at 5 months of age (that is, 4 months of HFD) and highlights a choline supplementation effect on the first predictive component (Fig. 1k,l). Quantifications all reflect an increase in TMA and TMAO in the HC-HFD in line with choline supplementation (Fig. 1m,n). In particular, the circulating TMA levels were similar in the CHD and the LC-HFD (0.38 μM in CHD vs 0.3 μM in LC-HFD) and were about 20 times lower than in the HC-HFD (5.9 μM). These results depict an increased microbial conversion of choline into TMA in our HC-HFD, an observation already made in a previous study[13]. These results suggest that TMA could mediate the metabolic and immune benefits of choline supplementation.

Baseline metabolic phenotyping after 2-month choline modulation in HFD

To further assess the impact of choline supplementation on metabolic homoeostasis and low-grade inflammation in HFD contexts, we performed a second experiment, feeding C57BL/6J mice a 60% kcal HFD with a time frame comparable to those used in subsequent experimental designs using osmotic minipumps for constant subcutaneous TMA

Fig. 1 | Choline supplementation improves glucose homoeostasis and inflammation after 5 months of HFD. Male mice were weaned at 3 weeks and fed a CHD diet before being randomly assigned to a CHD group (n = 68) or HFD group (n = 47) and monitored at 5 months of age. **a**, Effect of HFD feeding on GTT. **b**, Volcano plot of differentially expressed liver genes, highlighting that *Saa1* and *Saa2* are downregulated in HFD after 4 months of HFD. Red dots, significantly upregulated genes (false discovery rate (FDR) < 0.1); blue dots, significantly downregulated genes (FDR < 0.1). P values were corrected for multiple comparisons using the Benjamini–Hochberg method. **c**, Metabolic signature of diet on O-PLS model coefficient plot; line plot corresponds to covariance, and the colour scale represents proportion of variance explained. a.u., arbitrary units. **d**, Assessment of the contribution of factors diet and age on choline, TMA and TMAO by O-PLS variance components analysis: 5-week-old C57BL/6J mice were fed a CHD diet, a low-choline HFD or a low-choline HFD supplemented with choline (n = 10) and were phenotyped after 5 months. **e**, Plasma glucose concentration during an intraperitoneal GTT (ipGTT). **f**, Area under the curve of the plasma glucose concentration during an ipGTT. **g**, Body weight measured after 5 months of diet. **h**–**j**, Quantification of circulating cytokines: IL-6 (**h**), TNF (**i**) and IL-1β (**j**). **k**, Scores plot from a cross-validated O-PLS-DA model segregating the three groups of mice according to diet based on isotopic quantification of methylamines by UPLC–MS/MS; each component's explained variance is shown in parentheses. **l**, Empirical assessment of the significance of O-PLS goodness-of-fit parameters by generating a null distribution with 10,000 random permutations. **m**,**n**, Quantification of circulating TMA (**m**) and TMAO (**n**) by UPLC–MS/MS. Data are means; error bars, s.e.m. One-way ANOVA followed by Tukey's post hoc tests (superscript letters for factor levels, P < 0.05) on log-transformed data except **k** and **l**. Source data are provided.

https://doi.org/10.1038/s42255-025-01413-8

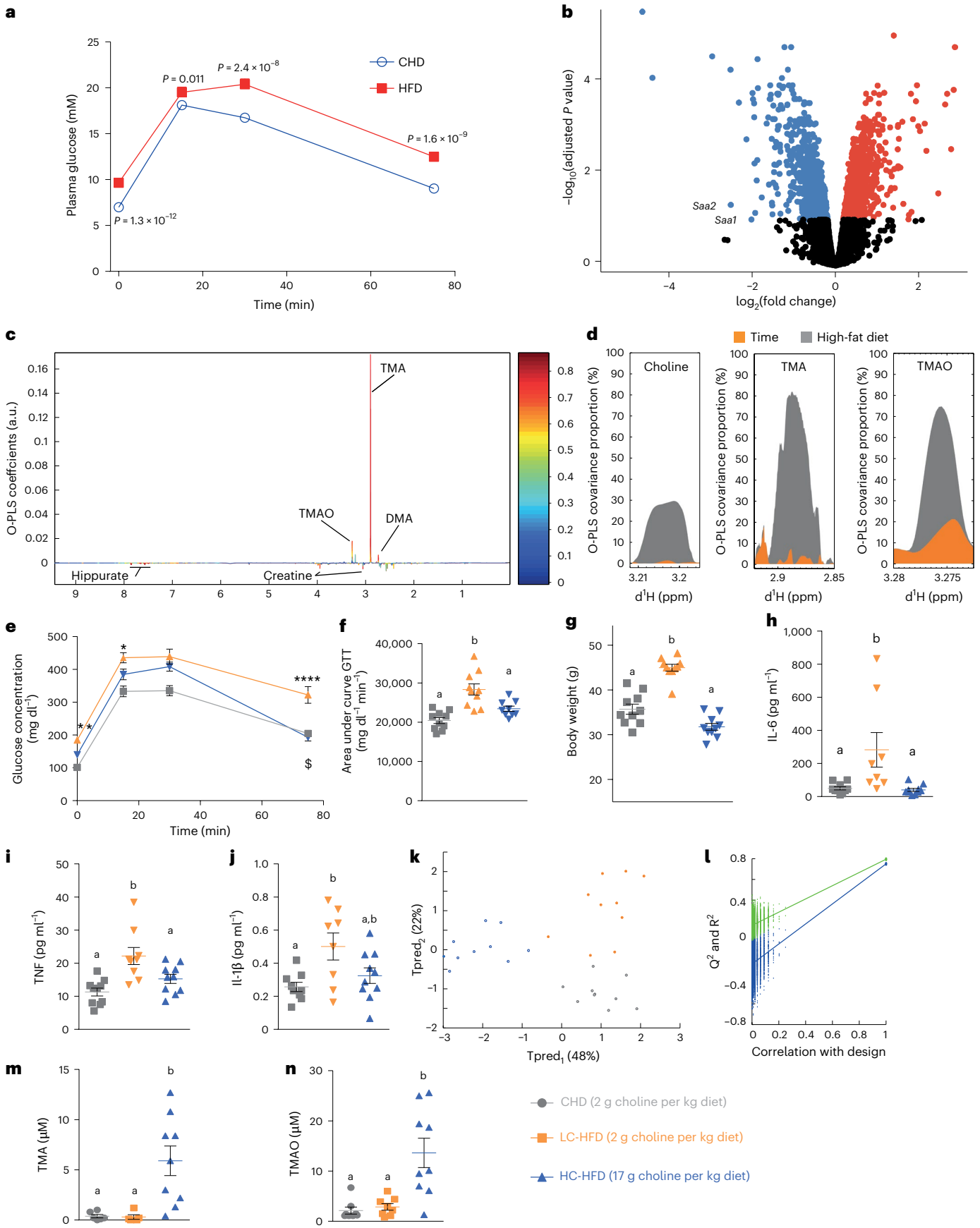

delivery. GTTs and weekly body weights showed a similar trend after 8 weeks of HFD feeding (Fig. 2a–d). Choline supplementation not only improved glucose tolerance (Fig. 2a,b) but also the Matsuda Index (Fig. 2c), a marker for IR derived from oral GTTs[31]. The normalization of insulin sensitivity was confirmed through insulin tolerance tests (ITTs) and insulin-induced hepatic Akt phosphorylation assays (Fig. 2e–h and Extended Data Fig. 3f for p-Akt/Akt ratio correction with β-actin). Notably, the normalization of insulin-induced hepatic AKT phosphorylation assays was primarily associated with a reduction of the basal level of p-Akt in HC-HFD compared to LC-HFD observed in saline conditions, demonstrating the reduction of IR (Fig. 2g). Indeed, it has been previously demonstrated that HFD increased the basal levels of p-Akt, and this contributes to IR[32]. We further characterized that HFD feeding increased hepatic NF-κB phosphorylation compared to CHD, which was normalized by choline supplementation, although this could also be a result of variable NF-κB protein levels between samples (Fig. 2i,j), a pattern that was also observed for expression of acute-phase proteins that are typically upregulated in response to tissue inflammation[33] (*Saa1*, *Saa2* and *Saa3*; Fig. 2k–m).

Chemical blockage of bacterial TMA biosynthesis and loss of metabolic benefits

To test whether the beneficial effects of choline supplementation are mediated by its microbial product TMA, we sought to block bacterial TMA production in HC-HFD-fed mice both non-specifically and specifically using a wide-spectrum antibiotics cocktail or 3,3-dimethyl-1-butanol (DMB), inhibiting microbial TMA-lyase[34], respectively. We first confirmed the functional blockage of TMA production in mice fed a HC-HFD, resulting in a drastic drop in circulating and excreted TMA and TMAO following 1% DMB administration (Extended Data Fig. 4a–d). In accordance with our hypothesis, both antibiotic and DMB treatments abolished the effects of choline supplementation-induced improvements in HFD, in particular for glucose tolerance, insulin sensitivity (as suggested by the Matsuda index; Fig. 3a–c and Extended Data Fig. 4e,f) and hepatic insulin sensitivity, as shown by the absence of a beneficial effect of choline supplementation on insulin-induced Akt phosphorylation (Fig. 3d,e and Extended Data Fig. 4g for β-actin normalization). The metabolic improvements associated with chemical TMA synthesis blockage were not a result of changes in body weight gain (Extended Data Fig. 4e), thereby strongly suggesting that the effects on glucose metabolism induced by inhibiting bacterial TMA production in HC-HFD were decoupled from obesity.

TMA treatment mimics choline supplementation

To further confirm whether TMA mediates the beneficial effects of choline supplementation, we chronically treated LC-HFD-fed C57BL/6J mice with TMA for 6 weeks using subcutaneous osmotic minipumps and assessed their immunometabolism. We confirmed that chronic TMA treatment at 0.1 mM in a LC-HFD did not affect body weight gain (Extended Data Fig. 4h) but effectively normalized glucose homoeostasis and the Matsuda Index, a readout of insulin sensitivity (Fig. 3f–h and Extended Data Fig. 4i). TMA treatment also improved the pro-inflammatory response to HFD feeding and hepatic expression of acute-phase proteins *Saa1*, *Saa2* and *Saa3* (Fig. 3i–l). These results suggest that chronic TMA treatment decouples body weight gain and adiposity from low-grade inflammation and glucose homoeostasis, thereby mimicking the immune and metabolic benefits observed in choline supplementation.

TMA is an IRAK4 kinase inhibitor

To identify a direct mechanism linking TMA to metabolic and immune benefits in HFD-fed mice, we sought to identify its host pharmacological targets. The kinome, made of 518 kinases encoded in the human genome[12], represents a repertoire of critical signal transduction switches for metabolic homoeostasis and inflammation. To discover specific physical interactions, we screened TMA against a panel of 456 clinically relevant human kinases using a high-throughput assay[35,36] (see Methods) and identified five preliminary hits for TMA (Fig. 4a and Supplementary Table 5). We then generated multiple-dose binding curves between TMA and each hit and confirmed that TMA physically binds IRAK4 (dissociation constant (K_d) = 14 nM; Extended Data Fig. 5a) but not the other four preliminary hits (flat dissociation curves with no K_d fit in Extended Data Fig. 5b–e, suggesting no physical binding was observed). Given that K_d only addresses a physical interaction in its simplest form (that is, binding), we functionally tested TMA as an IRAK4 inhibitor by quantifying IRAK4 kinase activity in the presence of ATP and increasing doses of TMA (see Methods) to derive a half-maximal relative inhibitory constant (IC_{50} = 3.4 μM; Fig. 4b) and an inhibitory constant K_i= 0.7 μM (see Methods). We also confirmed that choline, TMAO and DMB do not inhibit IRAK4 kinase activity (Extended Data Fig. 5f–h), and further verified that TMA does not inhibit IRAK1 (Extended Data Fig. 5i), as suggested by the phenotypic convergence of *Irak1*$^{-/-}$ mice fed a HFD, which were shown to have metabolic improvements similar to TMA treatment[37]. Nonetheless, this screen, combined with purified kinase activity assays, suggests that IRAK4 is the specific kinase target for TMA, which we next validated using a range of in vitro and in vivo experiments.

TMA inhibits IRAK4 signalling in human PBMCs and primary human hepatocytes

IRAK4 is a central kinase in the TLR pathway, sensing bacterial invasion and promoting a pyretic pro-inflammatory response in infectious contexts[38,39]. To further corroborate the inhibitory action of TMA on IRAK4 on innate immunity, we studied its effect on human peripheral blood mononuclear cell (PBMC) cytokine secretion and NF-κB signalling in response to LPS stimulation, a process exclusively mediated by IRAK4 downstream of TLR4, as previously demonstrated[38]. Consistent with this previous work, pre-treatment with TMA for 30 min dose-dependently blunted IL-6 and TNF secretion by PBMCs challenged with LPS after 4 h (Fig. 4c,d). Moreover, IL-6 and TNF secretion was virtually abolished by pre-treatment with the IRAK4-specific inhibitor PF06650833 (ref. 40) as an additional control (100 nM). Conversely, TMA (100 μM) or the IRAK4-specific inhibitor PF06650833 (100 nM) had no significant impact on TNF secretion by PBMCs stimulated by phorbol-ester/Ionomycin (Fig. 4e), similarly to human B cells harbouring IRAK4-inactivating mutations[41]. Taken together, these findings support our assertion that TMA acts through IRAK4 and further validate the functional inhibition of IRAK4 by TMA in innate immune cells. In addition, TMA (0.1 mM) significantly reduced IRAK1 phosphorylation at a site (Thr209) phosphorylated by IRAK4 (ref. 42) upon short-term stimulation of PBMCs with LPS (up to 60 min; Fig. 4f). TMA also inhibited ^{Thr209}IRAK1 phosphorylation dose-dependently after LPS stimulation of PBMCs (Fig. 4g) and, similarly, TMA time-dependently and dose-dependently suppressed NF-κBp65 phosphorylation in LPS-challenged PBMCs (Fig. 4h,i). In agreement with the cellular PBMC experiments, a single TMA dose significantly improved mouse survival in a 24 h LPS septic shock experiment (Fig. 4j), showing similar protection to IRAK4 kinase-inactive mice[43].

We then sought to test IRAK4 inhibition in a HFD context. The main free fatty acid in our HFD is palmitate, a saturated free fatty acid triggering TLR4 signalling. Therefore, we used a primary human hepatocyte model of low-grade inflammation and IR[44].

Under basal conditions (0 min), TMA (0.1 mM, 30 min) pre-treatment resulted in a significant decrease in $p^{Thr345/Ser346}$IRAK4/IRAK4, p^{Thr209}IRAK1/IRAK1 and $p^{Ser176/180}$IKKαβ/IKKβ. Palmitic acid (200 μM, 60 min) administration resulted in increased p^{Thr209}IRAK1/IRAK1, $p^{Ser176/180}$IKKαβ/IKKβ and p^{Ser536}NF-κBp65/NF-κBp65 (Extended

https://doi.org/10.1038/s42255-025-01413-8

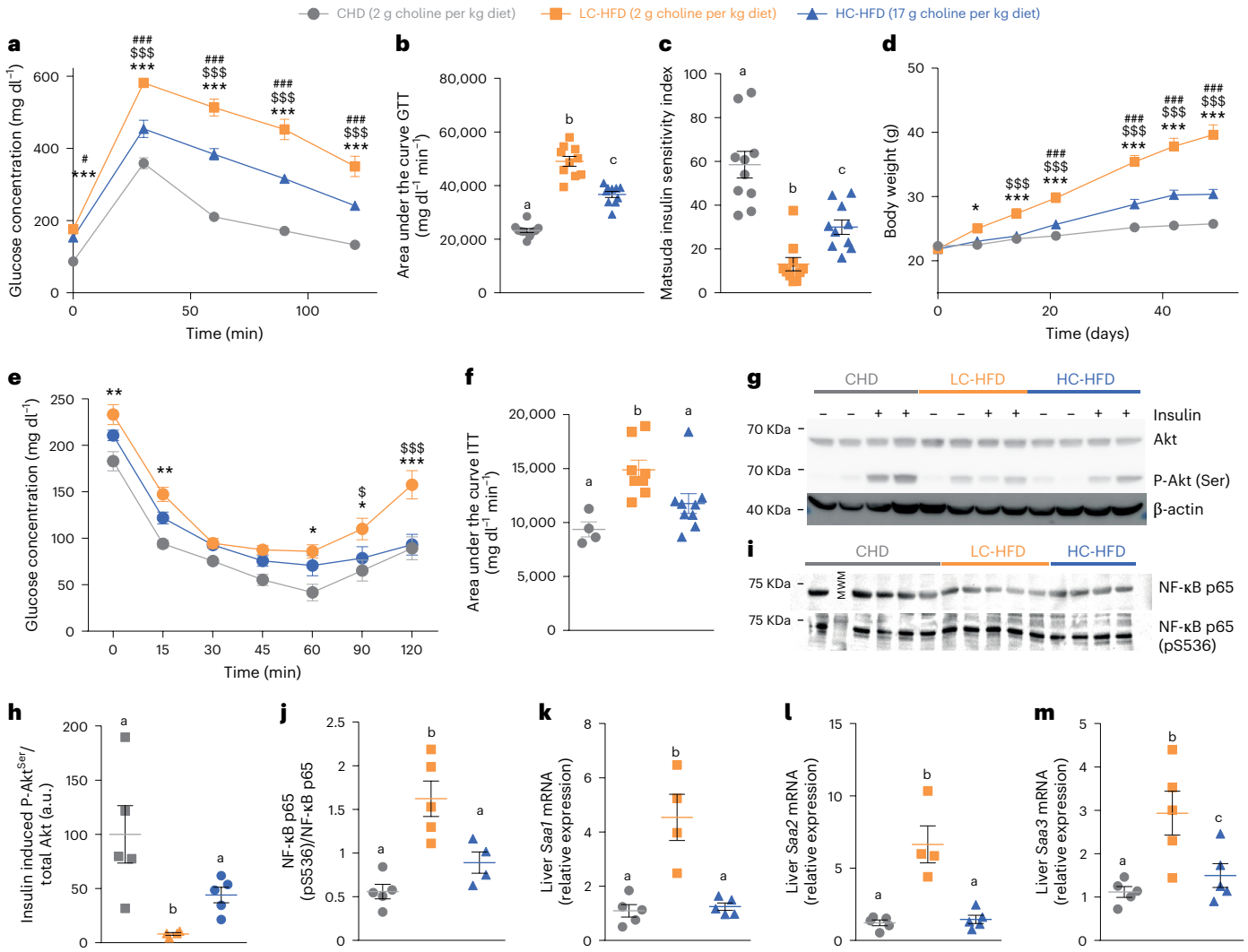

Fig. 2 | Choline supplementation corrects HFD adverse effects on glucose homoeostasis, insulin sensitivity and inflammation after 8 weeks of diet. C57BL/6J mice (5 weeks old) were fed CHD, LC-HFD or LC-HFD supplemented with choline ($n = 10$) and then phenotyped after 8 weeks. **a**, Plasma glucose concentration during an ipGTT. **b**, Area under the curve of the plasma glucose concentration during an ipGTT. **c**, Matsuda insulin sensitivity index calculated from the ipGTT. **d**, Body weight measured periodically during 8 weeks of diet. **e**, Plasma glucose concentration during an ipITT. **f**, Area under the curve of the plasma glucose concentration during an ipITT. **g**–**j**, Western blot analysis of liver Akt phosphorylation (**g**,**h**) and NF-kB phosphorylation (**i**,**j**). **k**–**m**, Expression of hepatic acute-phase inflammation proteins markers *Saa1* (**k**), *Saa2* (**l**) and *Saa3* (**m**). Data are means; error bars, s.e.m. In **c**, **d**, **f** and **h**–**m**, one-way ANOVA followed by Tukey's post hoc tests (superscript letters for factor levels, $P < 0.05$) on log-transformed data. In **a**, **b** and **e**, a non-parametric two-sided Mann–Whitney test was used for each time-point; significance comparison signs are as follows: (*) CHD vs LC-HFD; ($) LC-HFD vs HC-HFD; (#) CHD vs HC-HFD. Source data are provided.

Data Fig. 6a–d), which were normalized by TMA treatment. The TMA effect was significant as determined by a 2-way ANOVA for $p^{Thr345/Ser346}$IRAK4/IRAK4 ($P = 0.04$), p^{Thr209}IRAK1/IRAK1 ($P = 0.03$) and $p^{Ser176/180}$IKKαβ/IKKβ ($P < 0.001$). Normalization of the phosphorylation ratios in the TLR4 pathway by TMA resulted in a normalization of palmitic acid-induced IL-6 secretion in the cell medium after 4 h (Extended Data Fig. 6e). TMA also prevented the negative impact of palmitic acid (200 µM, 4 h) on insulin action (specifically on insulin-induced p^{Ser473}Akt1/Akt1), indicating a beneficial effect of TMA on insulin signalling (Extended Data Fig. 6f). TMA also tended to decrease $p^{Thr183/Tyr185}$SAPK/JNK/SAPK/JNK induced by palmitic acid (200 µM, 60 min; Extended Data Fig. 5j) but had no significant effect on p38MAPK (Extended Data Fig. 5k). Collectively, our results demonstrate that TMA is an IRAK4 kinase inhibitor ameliorating LPS inflammatory signalling in PBMCs and mice and normalizing palmitate-induced low-grade inflammation and aberrant insulin signalling in vitro, requiring further assessment in *Irak4*$^{-/-}$ mice.

Irak4$^{-/-}$ mice are protected against HFD-induced immune and metabolic dysregulations

IRAK4 is a key kinase required for defence against pyogenic infections in acute contexts[38,39]. To further test whether this kinase has a role in HFD-induced chronic low-grade inflammation and glucose homoeostasis, we fed 5-week-old *Irak4*$^{-/-}$ mice[45] and wild-type littermates on a C57BL/6J background (Extended Data Fig. 7a for genotyping) a LC-HFD, to avoid potential confounding effects from TMA for 8 weeks before assessing circulating cytokines, expression of hepatic inflammatory genes and acute-phase markers and metabolic homoeostasis (Fig. 5a–h). *Irak4*$^{-/-}$ mice presented improved glycemic control compared to wild-type littermates (Fig. 5a,b). Likewise, the inflammatory response to LC-HFD observed in wild-type mice was obliterated in *Irak4*$^{-/-}$ littermates (Fig. 5c–g). There was a similar trend for *Saa3* (Fig. 5h), but there was no effect on body weight gains (Extended Data Fig. 7b). Hence, similarly to TMA treatment, genetic ablation of IRAK4 abolishes the HFD-induced pro-inflammatory response and IGT, thereby decoupling

https://doi.org/10.1038/s42255-025-01413-8

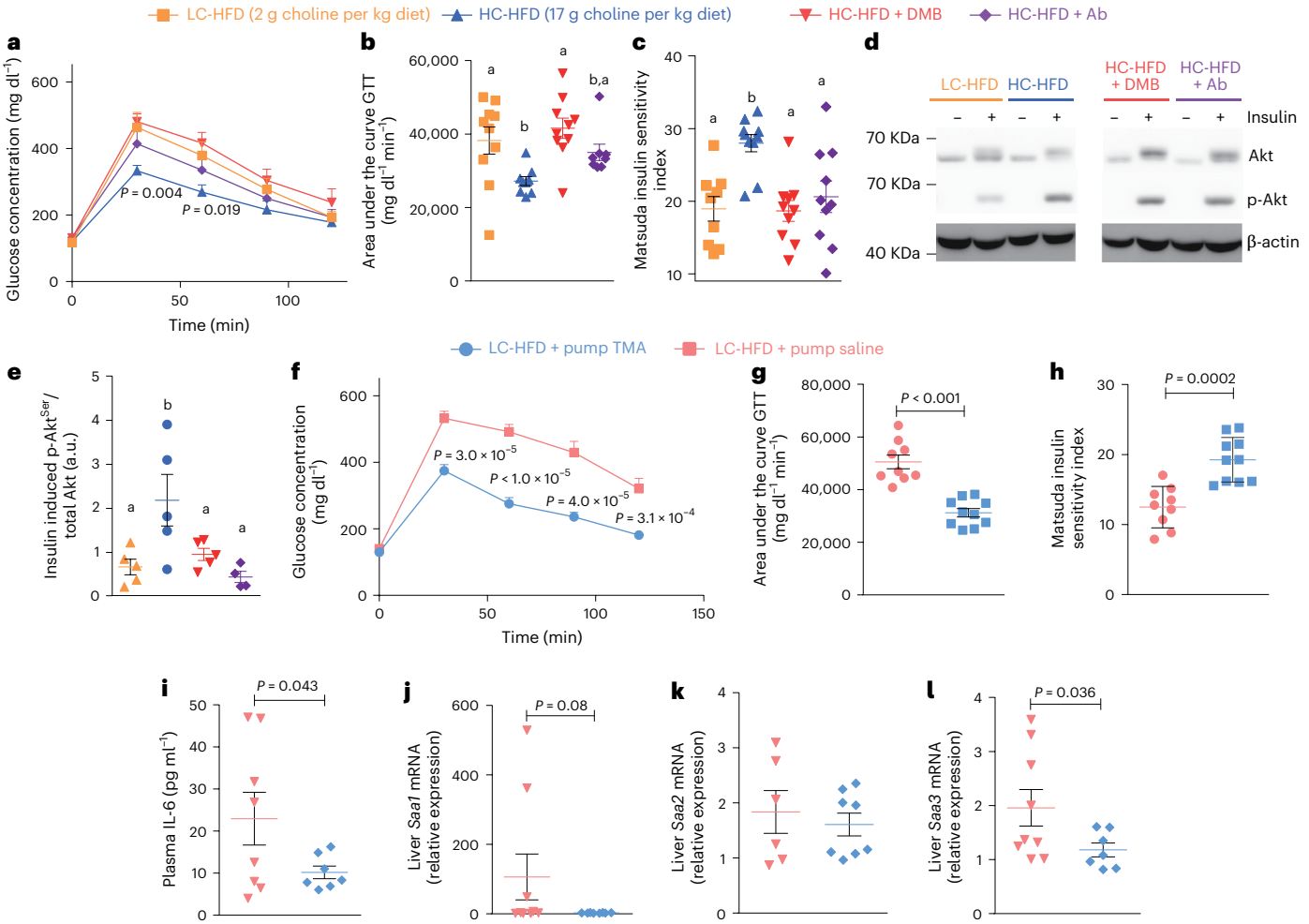

Fig. 3 | Blocking TMA production from choline cancels metabolic benefits from choline supplementation, and chronic TMA treatment mimics it. **a**–**e**, C57BL/6J mice (5 weeks old) were fed LC-HFD or LC-HFD supplemented with choline ($n = 10$). Two strategies were used in parallel to block TMA production from choline by the gut microbiota, using either 1% DMB in the diet or an antibiotic treatment. **a**, Plasma glucose concentration during an ipGTT. **b**, Area under the curve of the plasma glucose concentration during an ipGTT. **c**, Matsuda insulin sensitivity index calculated from the ipGTT. **d**,**e**, Western blot analysis of liver Akt phosphorylation. **f**–**l**, Mice were weaned at 3 weeks and fed a LC-HFD before being fitted with osmotic minipumps delivering a chronic circulating dose of TMA (0.1 mM) for 6 weeks ($n = 9$ saline HFD, $n = 8$ TMA HFD), with each data point representing a single mouse. **f**, Plasma glucose concentration during an ipGTT. **g**, Area under the curve of the plasma glucose concentration during an ipGTT. **h**, Matsuda insulin sensitivity index calculated from the ipGTT. **i**, Quantification of circulating IL-6. **j**–**l**, Expression of hepatic acute-phase inflammation protein markers *Saa1* (**j**), *Saa2* (**k**) and *Saa3* (**l**). Data are means; error bars, s.e.m. Results were assessed by one-way ANOVA followed by Tukey's post hoc tests (superscript letters for factor levels, $P < 0.05$) on log-transformed data.

obesity from IGT and low-grade inflammation with a similar phenotype to *Irak1* deficiency[37].

Pharmacological inhibition of IRAK4 normalizes glucose metabolism

Given that the *Irak4*$^{-/-}$ mice lack the whole protein, we compared the knockout phenotype with the phenotype of PF06650833, a recently discovered chemical inhibitor of the human IRAK4 protein[40] that has shown promising results in a phase-I trial for rheumatoid arthritis[46]. Treatment with PF06650833 improved body weight in LC-HFD mice (Extended Data Fig. 7c). This inhibitor also yielded significant improvements in plasma glycemia at the latter time-points of the GTT and ITT, and in cumulative glycemia (Fig. 5i–l), which was mirrored by an increase in Akt phosphorylation (Fig. 5m,n and Extended Data Fig. 7d for β-actin normalization). These results collectively show that specific chemical inhibition of IRAK4 leads to significant improvements in glycemic control, insulin sensitivity and insulin signalling. Moreover, the data suggest that IRAK4 could constitute a clinically relevant target in IR and related disorders.

Discussion

The discovery that TMA is a kinase inhibitor controlling IRAK4, a central kinase involved in innate immunity, is a major finding that provides an attractive mechanism for the metabolic and immune improvements observed with choline supplementation in HFD contexts (Fig. 6).

IRAK4 is the first regulatory checkpoint downstream of MyD88, the adaptor protein connecting IRAK4 to at least six TLRs sensing bacterial compounds or components[47]. IRAK4 deficiency is associated with bacterial infections in humans[39] and in mice[48]. Consistent with the involvement of the TLR signalling pathway at the crossroads between gut microbiota and dietary lipids[49,50], IRAK4 deletion and its inhibition by TMA and PF06650833 (ref. 40) rescued HFD-induced low-grade inflammation and IR[3,51,52], highlighting new and unexpected roles for this microbial metabolite and its target kinase in immunometabolism. The relative IC_{50} (3.4 µM) that we determined is half the plasma isotopic quantifications obtained by UPLC–MS/MS in the HFD group supplemented with choline. These quantifications are comparable to circulating TMA levels previously reported in normal human plasma, ranging between 0.42 and 48 µM (refs. 53,54), which makes this IC_{50}

https://doi.org/10.1038/s42255-025-01413-8

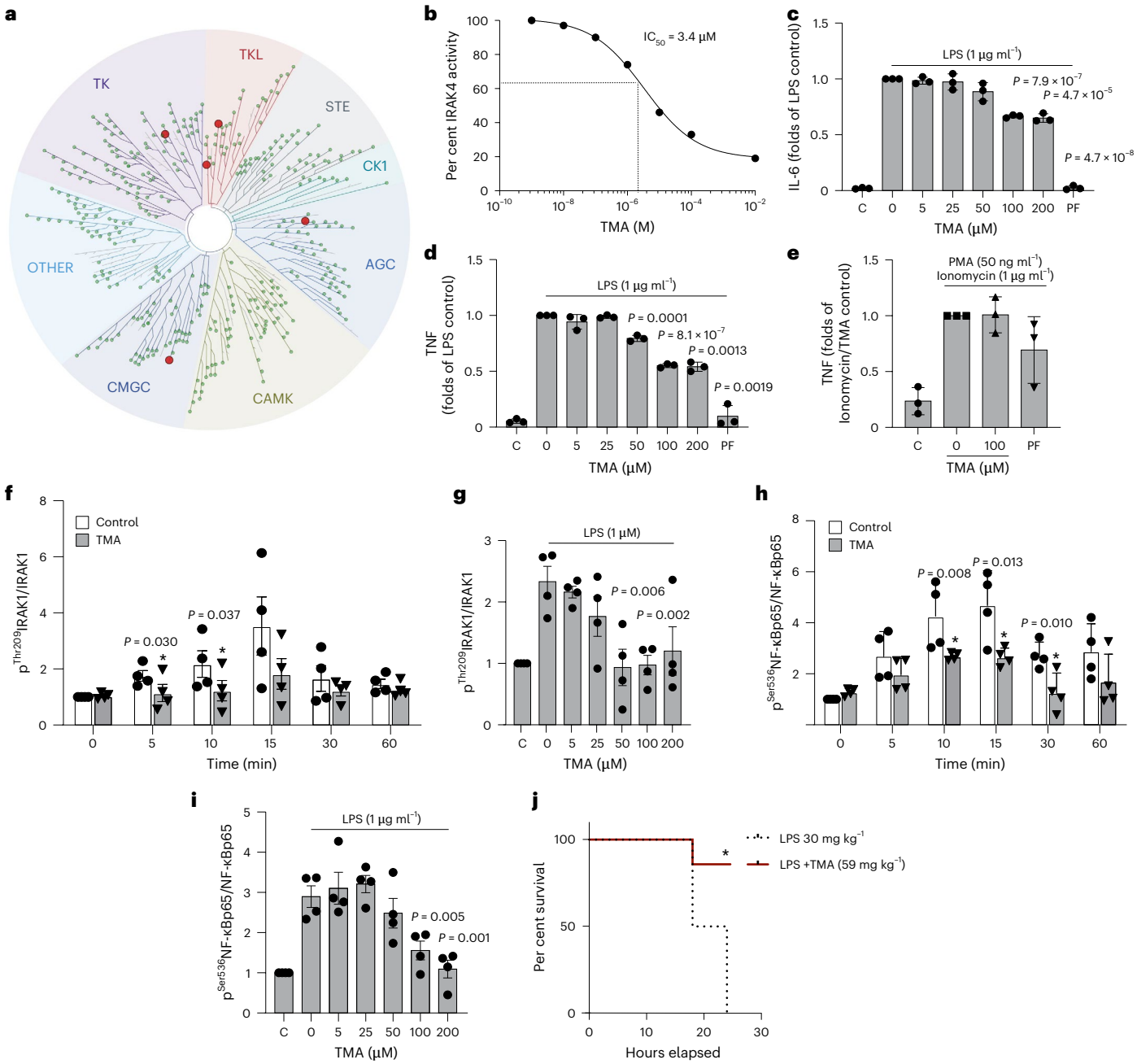

Fig. 4 | TMA inhibits IRAK4 and rescues LPS-induced TLR4-mediated pro-inflammatory response. a, Kinome screen for a single dose of TMA (0.1 mM) against 456 kinases. The kinases covered by the kinome scan assay are visualized using a phylogenetic layout. Preliminary positive hits with potential binding >35% vs control (DMSO) are represented by a red dot; non-binding kinases are represented by a green dot. Kinase group names: TK, tyrosine kinases; TKL, tyrosine kinase-like; STE, STE kinase group; CK1, cell linase 1; AGC, protein kinase A, G and C families; CAMK, calcium and calmodulin-regulated kinases; CMGC, CMGC kinase group. **b**, Functional characterization of the inhibition of IRAK4 by TMA. IRAK4 phosphorylation activity was determined in the presence of various concentrations of TMA and resulted in an IC_{50} of 3.4 µM. **c**,**d**, TMA preincubation (100 µM for 30 min) suppresses LPS-induced (1 µg ml^{-1}, 4 h) IL-6 (**c**) and TNF (**d**) release by human PBMCs. The values of the unstimulated controls were arbitrarily set to 1. For **c** and **d**, statistical significance ($P < 0.05$) was assessed with a two-sided unpaired Student's *t*-test (vs LPS-stimulated control). **e**, TMA (100 µM) or the IRAK4-specific inhibitor PF06650833 (50 nM) do not inhibit TNF secretion from human PBMCs after 4 h stimulation with PMA (50 ng ml^{-1}) and ionomycin (1 µg ml^{-1}). **f**, Impact of TMA pre-treatment (100 µM, 30 min) on human PBMCs' ^{Thr209}IRAK1/IRAK1 phosphorylation upon LPS (1 µg ml^{-1}) stimulation for the indicated times. **g**, Human PBMCs were pre-treated (for 30 min) with the indicated concentrations of TMA, and ^{Thr209}IRAK1/IRAK1 phosporylation was assessed after 10 min of LPS (1 µg ml^{-1}) challenge. The time-dependent (**h**) and dose-dependent (**i**) effect of TMA on phosphorylation of ^{Ser536}NF-κBp65/NF-κBp65 of human PBMCs stimulated with LPS (1 µg ml^{-1}) was assessed as in **f** and **g**. For **f**–**i**, the control value was arbitrarily set to 1, and statistical significance ($P < 0.05$) was assessed with a one-sided unpaired Student's *t*-test. For PBMC experiments in **c**–**i**, each data point represents a separate experiment. **j**, A 24 h Kaplan–Meier survival curve of mice challenged with a lethal dose of LPS (30 mg kg^{-1}) that received a single dose of TMA (59 mg kg^{-1}, red line), or vehicle (black line); *$P = 0.0047$ determined by two-sided log-rank Mantel–Cox test. Data are means; error bars, s.e.m.

https://doi.org/10.1038/s42255-025-01413-8

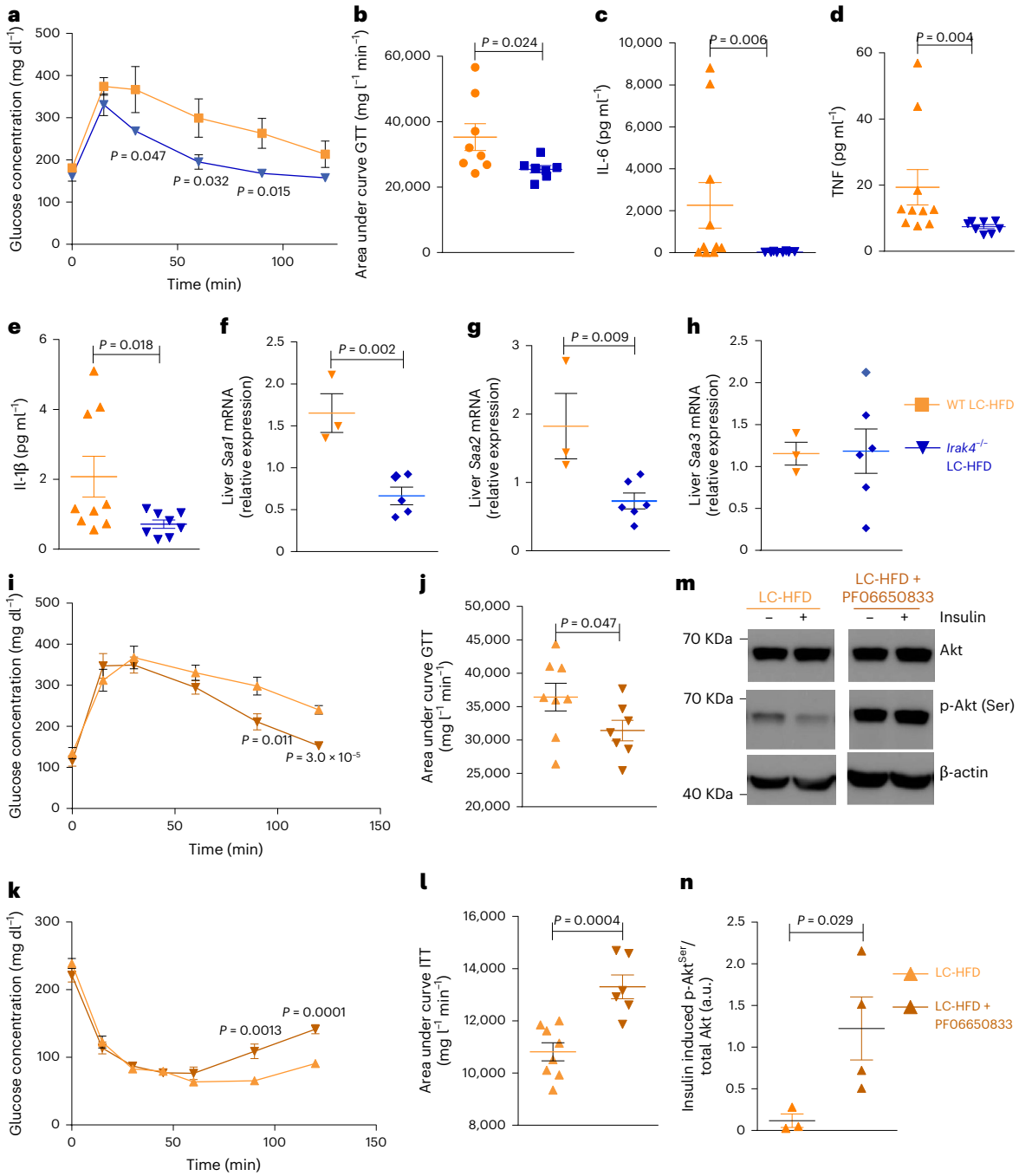

Fig. 5 | IRAK4 deficiency corrects IGT and pro-inflammatory response after 8 weeks of LC-HFD feeding in C57BL/6J mice, and a chemical inhibitor of IRAK4 mimics the effects on glucose homoeostasis. a–**h**, *Irak4*$^{-/-}$ mice and wild-type (WT) littermates (5 weeks old) were fed a LC-HFD (n = WT HFD and n = 8 *Irak4*$^{-/-}$ HFD) and were phenotyped after 8 weeks. Each point represents data from a single mouse. **a**, Plasma glucose concentration during an ipGTT. Two-sided Student's t-test (*P < 0.05). **b**, Area under the curve of the plasma glucose concentration during an ipGTT. **c**–**e**, Circulating cytokines IL-6 (**c**), TNF (**d**) and IL-1β (**e**). **f**–**h**, Liver mRNA expressions for *Saa1* (**f**), *Saa2* (**g**) and *Saa3* (**h**) genes. For **b**–**h**, data are means; error bars, s.e.m. Statistical significance (P < 0.05) was determined using a one-tailed Mann–Whitney test. **i**–**n**, Mice were weaned at 3 weeks and fed a LC-HFD before being fitted with osmotic minipumps delivering a chronic circulating dose of PF06650833 (50 nM) for 6 weeks. **i**, Plasma glucose concentration during an ipGTT. Each point represents data from a single mouse. **j**, Area under the curve of the plasma glucose concentration during an ipGTT. **k**, Plasma glucose concentration during an ipITT. **l**, Area under the curve of the plasma glucose concentration during an ipITT. **m**,**n**, Western blot analysis of liver Akt phosphorylation. A representative immune blot from n = 3 repeats is shown. Data are means; error bars, s.e.m. For **i**–**n**, P values were determined by one-sided unpaired Student's t-test (P < 0.05 was deemed statistically significant). For **n**, the data were log transformed.

particularly relevant with respect to pathophysiological mechanisms: dosing mice with 0.1 mM TMA was sufficient to improve inflammatory and metabolic responses. TMA can therefore be considered a 'microbial signalling metabolite'[55], sending a negative feedback signal to a pathway triggered by the influx of saturated free fatty acids in HFD contexts. This mechanism participates in maintaining a low immunological footprint and improved metabolic homoeostasis in a symbiotic relationship. The role of TMA as an IRAK4 inhibitor could, for instance, explain some of the beneficial effects reported for choline supplementation in patients with non-alcoholic fatty liver disease[56] as well as the improved

https://doi.org/10.1038/s42255-025-01413-8

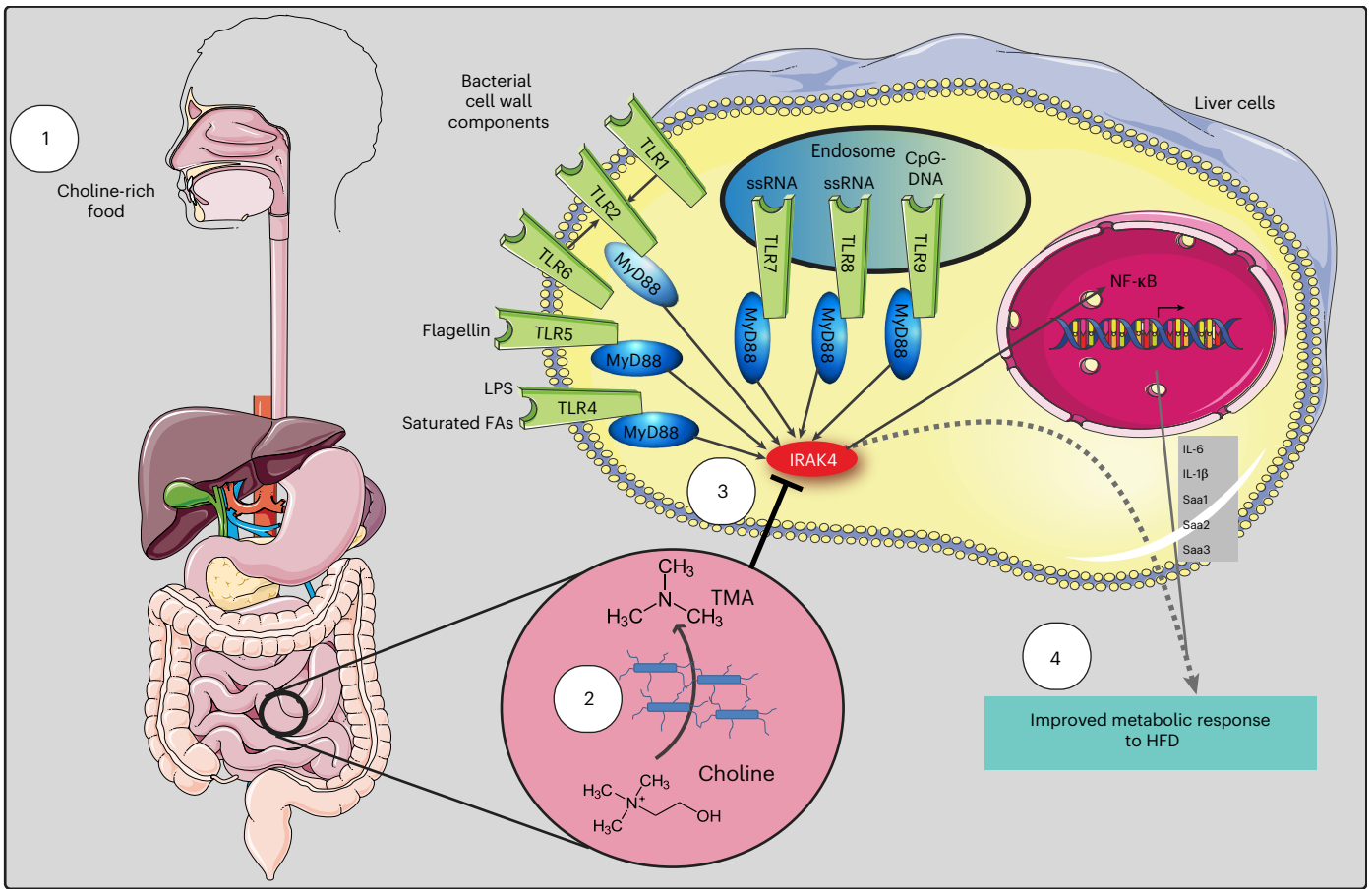

Fig. 6 | Overview of effects of IRAK4 inhibition by TMA on metabolic response to HFD. TMA is synthesized from dietary choline (1) by the gut microbiota (2) and specifically inhibits IRAK4 activity (3). This inhibition blunts the TLR signalling pathway (induced by LPS and saturated free fatty acids), leading to an improvement of metabolic response to HFD (for example, glucose homoeostasis). Image adapted from Servier Medical Art (https://smart.servier.com), licensed under CC BY 4.0 (https://creativecommons.org/licenses/by/4.0).

IR observed in those consuming higher choline diets in a healthy, genetically uniform human population[57]. Altogether, our results on IRAK4 inhibition and ablation provide further insight into the phenotypic convergence between *Myd88*, *Irak4* and *Irak1* knockout mouse models[37,58], suggesting that the gut microbiota, through TMA, proceeds with a targeted 'hijacking' of the TLR signal transduction machinery to the host's benefit, resulting in metabolic and immune improvements.

Our finding that TMA improves metabolic health in the context of HFD is surprising, given the extensive evidence linking higher levels of circulating TMAO (after phase-1 *N*-oxidation of TMA in the liver) with worse cardiovascular outcomes, particularly in patients with established atherosclerosis and thrombosis[14]. Our results show that the TMA-lyase inhibitor DMB blocks TMA production and abrogates the metabolic benefits brought about by choline supplementation in HC-HFD mice, suggesting that the benefits come from the conversion of choline to TMA.

Our findings are supported by the discovery that in diabetic mice, knockdown of the liver gene (*Fmo3*) that converts TMA to TMAO—an intervention that would increase TMA levels—improves IR and attenuates atherosclerotic burden[23]. Similarly, in an epidemiological study in a genetically homogeneous population, higher choline consumption was associated with improved insulin sensitivity[57].

Our work is consistent with the idea that TMA and TMAO may well have contrasting roles that are context-dependent and mechanism-dependent.

To illustrate context dependence, TMAO has different effects based on the insult. It has been linked to poor cardiovascular outcomes in humans; however, independently of its role in cardiovascular disease, it increases kidney fibrosis[59], beneficially reduces blood–brain barrier permeability[60] and is associated with improved survival outcomes in septic ventilated patients[61]. Moreover, TMAO levels in healthy adults did not predict future coronary events in a 10-year follow-up study[62], suggesting that in this context, TMAO might often require underlying pathology for its detrimental effects to become overt. Contrary to coronary heart disease, in which significant evidence points towards a detrimental role by TMAO[63] for obesity-driven IR and dysregulated glucose handling (which is the main focus of this work), the role of TMAO is unclear, with conflicting human studies pointing to protective[28,64], detrimental[65] or insignificant[66,67] TMAO effects. Mice fed a choline-enriched (1%) CHD showed IGT compared to those on a CHD and impaired β cell function, owing to increased plasma TMAO[68], in an apparent contradiction to our results in HFD-challenged mice. We have demonstrated a similar diet-dependent phenomenon with the host-microbiome co-metabolite hippurate, whereby hippurate improved glucose handling and IR only in mice fed a HFD[69]. Similarly, TMA has shown context dependence, negatively affecting the blood–brain barrier[60] and endothelial vasoconstriction[70].

To illustrate the mechanism dependence, TMAO augments Ca^{2+}-mediated platelet aggregation after thrombin treatment. TMAO also binds to and activates purified protein kinase RNA-like ER linase (PERK), while structurally related metabolites such as choline do not[71]. This proatherothrombic mechanism may well explain the adverse cardiovascular outcomes associated with TMAO[13,16]. Conversely, it has been shown that FMO3 inactivation, preventing *N*-oxidation of TMA and therefore increasing TMA compared to TMAO, leads to several beneficial metabolic outcomes[21–24]. Consistent with our observations,

Fmo3 deletion prevented hyperglycaemia, hyperlipidemia and atherosclerosis in mice and is considered a target for dysmetabolism[23]. Such a protective role for FMO3 inactivation cannot be explained by TMAO removal alone and therefore points to an independent mechanism for TMA.

Our discovery that TMA binds to and inhibits IRAK4, whereas TMAO does not, provides an unexpected and independent mechanism of action for TMA. Our observations on IRAK4 inhibition by TMA and in *Irak4* knockout mice are consistent with observations in Myd88 and *Irak1* knockout mice, resulting in improved glucose tolerance and insulin sensitivity. Collectively, we submit that our study reveals a context-dependent and target-specific mechanism of action independently of the proatherothrombic mechanism reported for TMAO in an HFD context. Modifying the TMA/TMAO ratio, for example, through FMO3 inhibition, would remove the deleterious proatherothrombic effect reported for TMAO and, through increased TMA concentration, would also blunt low-grade inflammation and improve glucose homoeostasis, in accordance with both mechanisms.

Our study is not without limitations. Notably, the derived IC_{50} from the purified kinase activity assay was approximately 250-fold higher than the K_d derived from the kinase screen. This may be a result of (1) the different properties reported upon by the different assay (physical binding for K_d, activity for half-maximal inhibition for IC_{50}); (2) the experimental design of the assays (IRAK4 bound to a drug-ligand versus ATP binding); (3) different kinase expression systems (bacterial *E. coli* versus insect Sf9 cells) and therefore potentially diverging IRAK4 catalytic activities (see Methods). Furthermore, the kinase screen tested 456 kinases out of the 518 kinases identified in the human kinome[12], leaving the possibility that one of the 62 unscreened kinases could be indirectly involved, regardless of our focus on IRAK4-mediated LPS-signalling and HFD-signalling, which is consistent with established literature. Additionally, for the IRAK4 activity kinase assay, we used a relatively low ATP concentration (50 µM), which is orders of magnitude lower than the concentration in cells. Moreover, we did not calculate K_i at varying ATP concentrations. Instead, we used an IRAK4-ATP K_m derived from the literature (Methods), which may have affected the accuracy of the K_i that we report (0.7 µM). Using more stringent conditions (K_i of 3 µM, ATP K_m of 500 mM and assuming a cellular ATP concentration of 1–5 mM) would result in a cellular TMA IC_{50} for IRAK4 in the range of 9–30 µM, at the high end of physiological concentrations for TMA. We previously demonstrated in animals that plasma TMA concentrations can dramatically increase after a meal[19], suggesting that TMA effects could be observed at the postprandial phase. Together with our findings here, this highlights how different meals rich in TMA precursors can affect plasma TMA levels, which will be tested in a human dietary intervention study. Despite the intrinsic limitations of the kinase assays, our work highlights the pathophysiological relevance of IRAK4 inhibition by TMA in two distinct cellular models (primary human hepatocytes and PBMCs) and four in vivo mouse models (LPS septic shock, HC-HFD, TMA supplementation and *Irak4* knockout) with TMA concentrations comparable to those found in human plasma, making these results biologically meaningful.

In conclusion, through the combination of ex vivo, in vitro and in vivo approaches, we reveal a unique mechanism in which TMA acts as a gut microbial signalling metabolite inhibiting IRAK4, a central molecular target in the TLR pathway, thereby allowing the gut microbiota to control HFD-induced pro-inflammatory response(s) and IR. The kinome represents a key repertoire of regulatory host targets for microbial signals, and the uncharted microbiome–kinome crosstalk requires further investigation. Our work can guide human trials in which the efficacy of IRAK4 inhibitors available for human use or dietary interventions that increase TMA bioavailability can be evaluated in the context of obesity and IR. Moreover, given that IR is an independent risk factor of cardiovascular disease in humans[72], our work uncovers a strategy to alleviate obesity-associated increased cardiovascular risk. By highlighting the physiological and therapeutic roles of TMA and IRAK4 on HFD-induced low-grade inflammation and IR, we anticipate that its immunomodulatory properties extend past IR to a wider range of human pathologies involving TLR signalling and modulation of innate immunity.

Methods

Protocols

All experimental procedures involving mice were carried out in accordance with UK Home Office, Canadian Council on Animal Care, the Ethics Committee of the French Research Ministry (authorization number 00486.01), Belgian Law of May 29, 2013 regarding the protection of laboratory animals (agreement number LA1230314) and local guidelines on animal welfare and license conditions and the University of Oxford, University of Ottawa, Université Pierre et Marie Curie and Université catholique de Louvain guidelines on animal welfare.

PBMC isolation and cell-based assays

PBMCs were isolated by our established method[73], following local ethical approval from Imperial College Research Ethics Committee (19IC5372). Human peripheral blood samples (32 ml) were collected from donors in BD Vacutainer Cell Preparation Tubes containing Sodium Heparin/Ficoll (BD Biosciences). PBMCs were separated by centrifugation at 1600*g* for 30 min at room temperature (20–22 °C), followed by three washing steps with PBS and 10% FBS (LabTech) and centrifuged at 520 RCF for 10 min after each wash. Viability was measured using the Alamar Blue assay. Donors were females, aged between 25 and 32 years. All subjects were healthy volunteers by self-declaration and provided written informed consent.

LPS stimulation and IL-6 and TNF release quantification

Human PBMCs (1×10^5 per condition in duplicate), freshly isolated as described above, were serum-starved in 0.1% v/v FCS RPMI-1640 (Sigma-Aldrich, R7638) in the presence of TMA (Sigma-Aldrich, 72761) or the IRAK4 inhibitor PF06650833 (0.5 µM; Tocris, 6373) for 30 min, as indicated in the corresponding figures. PBMCs were subsequently stimulated with 1 µg ml^{-1} LPS (Sigma-Aldrich, L2630) for 4 h (37 °C, 5% CO_2). For the phorbol 12-myristate 13-acetate (PMA)/ionomycin stimulation experiments, human PBMCs isolated as above (1×10^5 per condition) pre-incubated with TMAO (100 µM), PF06650833 (0.5 µM) or vehicle as indicated for 30 min were then stimulated with 50 ng ml^{-1} PMA (Sigma-Aldrich, 79346) and 1 µg ml^{-1} ionomycin (Sigma-Aldrich, I0634) for 4 h. Next, cells were pelleted by centrifugation (200*g* for 10 min), and supernatants were collected and stored at −20 °C until further use. IL-6 and TNF were measured in the media diluted 1:10 in RPMI-1640 using the DuoSet ELISA kits (R&D, DY206 and DY210, respectively) according to the manufacturer's instructions. For PMA/ionomycin TNF measurements, the media were undiluted. For all treatments, $n = 4$ biological repeats.

PBMCs IRAK1 and NF-κBp65 phosphorylation in response to LPS

Freshly isolated human PBMCs (1×10^6 per ml per condition) were added to 96-well plates coated with L-poly-lysine for 30 min (100 ng ml^{-1}; Sigma-Aldrich, P4707) in RPMI-1640 containing 20% FCS and were left to attach to the wells overnight at 37 °C, 5% CO_2. The following day, media were discarded and cells were incubated in serum-free RPMI-1640 containing 100 µM TMA, or RPMI-1640 vehicle for 30 min. PBMCs were then stimulated with LPS (1 µg ml^{-1}) for up to 60 min (times indicated in the corresponding figure legends). At the end of the stimulation, PBMCs were fixed with 8% paraformaldehyde (Sigma-Aldrich, F8775) at room temperature for 20 min. Phosphorylation of IRAK1 (at Thr209) or NF-κBp65 (at Ser536) was determined in fixed PBMCs using commercially available ELISA kits (LSBio, LS-F1401-1 or LS-F891-1, respectively) according to the manufacturer's instructions.

Readings were normalized to the levels of total IRAK1 protein determined in sister wells, which were treated identically. The dose-dependent impact of TMA (see corresponding figures) on phosphorylation levels of IRAK1 or NF-κBp65 upon LPS (1 μg ml^{-1}) stimulation of PBMCs (for 10 min or 15 min, respectively) was also determined using the commercially available kits from LSBio as described above.

Cell-based assays in primary human hepatocytes

Cryopreserved primary human hepatocytes were commercially sourced (Innoprot) and cultured with hepatocytes medium (Innoprot) supplemented with 5% FBS, 1% hepatocytes growth supplement (mixture of growth factors, hormones and proteins necessary for culture of primary hepatocytes) and 100 U ml^{-1} penicillin and streptomycin. Human hepatocytes were grown on poly-L-lysine pre-coated cell dishes at 37 °C and a 5% CO_2 atmosphere following the manufacturer's recommendations. The following experiments were performed 24 h after seeding: first, palmitic acid (200 μM) administration (0 and 60 min) with or without TMA (0.1 mM, 30 min) pre-treatment, plus co-administration during palmitic acid exposure were assayed. The palmitic acid solution was prepared as previously reported[44,74]. In this experiment, the effect of palmitic acid and TMA on IRAK1, IRAK4, NF-κBp65, IKKαβ, SAPK/JNK and p38MAPK activity was analysed. In a second experiment, the effect of TMA (0.1 mM, 30 min) pre-treatment plus co-administration during vehicle or palmitic acid exposure for 4 h on insulin action and on IL-6 release was tested. Insulin action was evaluated by measuring p^{Ser473}Akt1/Akt1 after insulin (100 nM, 10 min) stimuli.

p^{Thr209}IRAK1, total IRAK1, p^{Ser536}NF-κBp65, total NF-κBp65, p^{Ser473}AKT1, total AKT1 and GAPDH (as an endogenous control) were measured with specific colourimetric cell-based ELISA Kits (Assay Biotechnology Company, CytoGlow IRAK1 (CBP1425), CytoGlow NF-κBp65 (CBP1633) and CytoGlow AKT1 (CBP1490), following the manufacturer's instructions. For data analysis, the optical density of target proteins (read at 450 nm) was normalized with cell nuclei crystal violet staining (read at 595 nm), which was proportional to cell counts. The analysis of cell-based assays was performed in a blind manner.

p$^{Thr345/Ser346}$IRAK4/IRAK4, p$^{Ser176/180}$IKKαβ/IKKβ, p$^{Thr183/Tyr185}$SAPK/JNK and p$^{Thr180/Tyr182}$p38MAPK/p38MAPK were determined by western blot. In brief, hepatocyte proteins were directly extracted in radioimmunoprecipitation assay (RIPA) buffer (0.1% SDS, 0.5% sodium deoxycholate, 1% Nonidet P-40, 150 mM NaCl and 50 mM Tris-HCl pH 8.0) supplemented with protease inhibitors (1 mM phenylmethylsulfonyl fluoride). Cellular debris and lipids were eliminated by centrifugation of the solubilized samples at 13,000 rpm for 10 min at 4 °C, recovering the soluble fraction. Protein concentration was determined using the RC/DC Protein Assay (Bio-Rad Laboratories). RIPA protein extracts (20 μg) were separated by SDS–PAGE and transferred to nitrocellulose membranes by conventional procedures. Membranes were immunoblotted with antibodies against the following proteins: p$^{Thr345/Ser346}$IRAK4 (11927), IRAK4 (4363), p$^{Ser176/180}$IKKαβ (2694), IKKβ (8943), p$^{Thr183/Tyr185}$SAPK/JNK (4668), SAPK/JNK (9258), p$^{Thr180/Tyr182}$ p38MAPK (9215) and p38MAPK (9212), all purchased from Cell Signaling Technology, and β-actin (sc-47778, Santa Cruz Biotechnology). Anti-rabbit IgG and anti-mouse IgG coupled to horseradish peroxidase was used as a secondary antibody. Horseradish peroxidase activity was detected by chemiluminescence, and quantification of protein expression was performed using Scion Image software. IL-6 concentration in hepatocyte media was measured using Human IL-6 Quantikine ELISA Kit (R&D Systems, D6050). All experiments were performed with at least three sample replicates.

Mouse models

Longitudinal HFD feeding in mice. All experiments were approved by the ethical committee of the University of Oxford. Male mice from a C57BL/6J inbred strain were bred in our animal facility by using a stock originating from The Jackson Laboratory. At 5 weeks of age, groups of eight to ten mice were transferred to a 40% w/w HFD (65% kcal) (Special Diets Services, 824155b), containing 32% lard and 8% corn oil, whereas control groups remained on a normal carbohydrate (CHD) diet containing 5% fat, 19% protein and 3.5% fibre (B&K rat and mouse pelleted diet, B&K Universal) for up to 6 months. Detailed diet formulations were published previously[13] and are summarized in Supplementary Table 6.

Mice were housed under a 12 h–12 h light–dark cycle. For physiological profiling, several mouse groups fed CHD or HFD were tested to assess the consistency of results and discard any impact of potential batch effects. Intraperitoneal GTTs were performed on 2, 3, 5 and 7-month-old mice after an overnight fast, as previously published[75] (see also metabolic phenotyping below). Then, 4 days after the GTT, 24 h urinary samples (09:00–21:00 h) were collected from mice maintained in individual metabolic cages. Urinary samples collected in a solution of 1% (wt/vol) sodium azide were centrifuged to remove solid particles and kept at −80 °C until assayed. After an overnight fast, mice were killed by exsanguination. Plasma was separated by centrifugation and stored at −80 °C until ^{1}H-NMR analysis.

Choline supplementation on HFD. At 5 weeks of age, mice were fed either a CHD containing 2 g of choline per kg of diet (Research Diets, D12450J), a LC-HFD containing 2 g of choline per kg of diet (Research Diets, D12492), a HC-HFD containing 17 g of choline per kg of diet (Research Diets, D16100401), a HC-HFD containing 1% of DMB or a HC-HFD combined with a cocktail of antibiotics (0.5 g l^{-1} vancomycin hydrochloride, 1 g l^{-1} neomycin trisulfate, 1 g l^{-1} metronidazole, 1 g l^{-1} ampicillin sodium) in drinking bottles (n = 6–10 per group) for 8 weeks (see diet formulations in Supplementary Table 6). Mice were then killed by decapitation, and organs were dissected and weighed.

***Irak4*$^{-/-}$ mice.** *Irak4*$^{-/-}$ mice on a C57BL/6J background, as previously described[38,45], were bred with C57BL/6J mice (The Jackson Laboratory), and the F1 offspring were subsequently bred to produce the *Irak4*$^{-/-}$ mice and wild-type littermates used for this study. Mice were bred and genotyped at the Animal Facility of the University of Ottawa Heart Institute. The following primers were used for genotyping. *Irak4* knockout, 5′-TGAATGGAAGGATTGGAGCTACGGGGGT-3′; *Irak4* common, 5′-GAACACGCTCCCAGGTCTCTTTCCAAC-3′; and *Irak4* wild-type, 5′-TCTTCTACCTGAAATATGAAAGATTCCT-3′. The PCR reaction was run at 94 °C for 60 s, 60 °C for 60 s and 72 °C for 60 s for 40 cycles. The mice (10–12 weeks old) were fed with HFD for 8 weeks and then killed by decapitation, and their organs were dissected and weighed at the end of the study.

Chronic TMA and PF06650833 treatment in LC-HFD-fed mice. C57BL/6J mice (Charles River; 5 weeks old) were housed for 1 week before the experiment in a controlled environment. Mice were maintained under a 12 h–12 h light–dark cycle. On day 0, the 10-week-old mice were anaesthetized with isoflurane (ForeneH, Abbott). Mini-osmotic pumps were implanted subcutaneously (Model 2006, Alzet) (flow rate, 0.15 ml h^{-1}; total filling volume, 200 ml; delivery duration, 42 days) as previously described[76]. The osmotic mini-pump contained either vehicle or TMA (0.1 mM in circulation) or PF06650833 (50 nM in circulation). After 6 weeks of metabolite treatment, mice were killed by decapitation, and the organs were dissected and weighed.

Septic shock mouse model. Male mice on a C57BL/6J background (6 weeks old) were purchased from Charles River and maintained in a controlled environment for 2 weeks to acclimate them to local conditions. The animal experimental protocol was approved by local and national committees in charge (Tor Vergata University Institutional Animal Care and Use Committee and Ministry of Health, license no. 265/2019-PR) and conducted in accordance with accepted standards of humane animal care. Mice were intraperitoneally injected with

59 mg kg^{-1} TMA (Sigma-Aldrich, 72761) (treatment group, $n = 7$) or PBS alone (control group, $n = 6$) 30 min before LPS injection (30 mg kg^{-1} of LPS (Sigma-Aldrich, L2630) in sterile PBS by intraperitoneal injection). The survival of the mice was monitored every 4 h for 36 h.

Mice were housed in standard ventilated cages under a 12 h–12 h light–dark cycle at 20–23 °C and 40–60% humidity. For mouse experiments, staff who were responsible for phenotyping and biospecimen collection also handled the dietary intervention; therefore, they were not blinded to experimental conditions.

Physiological phenotyping

After 4 weeks of treatment, an intraperitoneal GTT test (2 g kg^{-1}) was performed in conscious mice following an overnight fast. Blood was collected from the tail vein before glucose injection and 30, 60, 90 and 120 min afterwards. Blood glucose levels were determined using an Accu-Check Performa (Roche Diagnostics). Additional blood samples were collected at baseline and 30 min after glucose injection in Microvette CB 300 Lithium Heparin (Sarstedt). Plasma was separated by centrifugation and stored at −80 °C until the insulin radioimmunoassay. Circulating insulin levels were determined using insulin ELISA kits (Mercodia). The Matsuda insulin sensitivity index was calculated as previously published[31].

After 5 weeks, we performed an ITT. Mice that had been fasted for 5 h were injected intraperitoneally with insulin (0.75 mU g^{-1}; Actrapid, Novo Nordisk). Blood glucose levels were measured immediately before and 15, 30, 45, 60, 90 and 120 min after insulin injection with a standard glucose meter (Accu-Check, Roche) on the tip of the tail vein.

Gene expression

Groups of six mice showing consistent pathophysiological profiles in response to CHD or HFD treatment were selected for microarray analysis performed with our established method[75], and data were deposited in ArrayExpress under accession number E-MEXP-1755. Total RNA was isolated from frozen liver tissue using the Trizol reagent (Invitrogen Life Technologies), followed by further purification with RNeasy spin columns (Qiagen). The concentration and quality of RNA samples were evaluated using an Agilent 2100 Bioanalyser (Agilent Technologies). Gene expression analysis was performed using the Affymetrix Mouse Genome arrays (U430A and U430B). These arrays include 22,690 (U430A) and 22,576 (U430B) probe sets, enabling the detection of transcript levels for approximately 13,250 (U430A) and 7,577 (U430B) unique genes and expressed sequence tags. For each sample, 10 µg of total RNA was used for first-strand cDNA synthesis, followed by in vitro transcription to generate biotin-labelled complementary RNA (cRNA). The cRNA samples were then assessed for yield and integrity using an Agilent 2100 Bioanalyser. After fragmentation, individual cRNA preparations were hybridized to the microarrays using a temperature-controlled Affymetrix hybridization oven. Post-hybridization washing and staining were carried out using the Affymetrix Fluidics Station 450. Finally, the arrays were scanned at a wavelength of 560 nm with an Agilent scanner (Affymetrix). The Bioconductor[77] package Limma[78] was used to generate the list of differentially expressed genes. Gene ontology was implemented using Enrichr[79], and signalling pathway impact analysis was conducted using SPIA[80].

For qPCR analysis, total RNA was prepared from tissues using TriPure reagent (Roche). Quantification and integrity analysis of total RNA were performed by analysing 1 µl of each sample in an Agilent 2100 Bioanalyzer (Agilent RNA 6000 Nano Kit). cDNA was prepared by reverse transcription of 1 mg total RNA using a Reverse Transcription System kit (Promega). Real-time PCR was performed with the StepOnePlus real-time PCR system and software (Applied Biosystems) using Mesa Fast qPCR (Eurogentec) for detection according to the manufacturer's instructions. RPL19 RNA was chosen as the housekeeping gene. All samples were performed in duplicate in a single 96-well reaction plate, and data were analysed according to the $2^{-\Delta\Delta CT}$ method. The identity and purity of the amplified product were assessed by melting curve analysis at the end of amplification. The primer sequences for the targeted mouse genes are as follows: SAA1 forward, CATTTGTTCACGAGGCTTTCC; SAA1 reverse, GTTTTTCCAGTTAGCTTCCTTCATGT; SAA2 forward, GGGGTCTGGGCTTCCCATCT; SAA2 reverse, CCATTCTGAAACCCTTGTGG; SAA3 forward, CGCAGCACGAGCAGGAT; SAA3 reverse, CCAGGATCAAGATGCAAAGAATG as previously reported[81]. Quantitative PCR with reverse transcription assays were performed in a single batch, with the personnel blinded to treatment groups.

Circulating cytokine quantification

Circulating cytokines were quantified using the MSD V-PLEX Plus Proinflammatory Panel 1 kit. Plasma samples were diluted two times in the diluent provided, and the experiment was processed as outlined by the manufacturer and read on a SECTOR imager 2400. Cytokine assays were performed in a single batch with the personnel blinded to treatment groups.

Western blotting

Western blot analyses were performed according to our established methods[82]. To analyse the insulin signalling pathway, mice were allocated to either a saline-injected subgroup or an insulin-injected subgroup so that both subgroups were matched in terms of body weight and fat mass. They then received 1 mU insulin per g body weight (Actrapid; Novo Nordisk) or an equal volume of saline solution. Then, 3 min after injection, the mice were killed and their liver was dissected. A total of 30 mg of liver was homogenized in 680 µl of RIPA buffer containing a cocktail of protease and phosphatase inhibitors. The homogenate was then centrifuged at 12,000*g* for 20 min at 4 °C. Equal amounts of proteins were separated by SDS–PAGE and transferred to nitrocellulose membranes. Membranes were incubated overnight at 4 °C with antibodies diluted in Tris-buffered saline Tween-20 containing 1% BSA:p-Akt Ser473 (1:1,000; Cell Signaling Technology, 4060), total Akt (1:1,000; Cell Signalling Technology, 9272S), p-NF-κB (1:3,000; AbCam, ab86299) and total NF-κB p65 (1:3,000; Cell Signalling Technology, 8242). Insulin-induced p-Akt/total Akt corresponds to the ratio between p-Akt/Akt in insulin-treated mice and p-Akt/Akt in saline-treated mice. For these western blots, the membranes were stripped and re-probed with a β-actin antibody as a loading control. In separate densitometric analyses, we additionally corrected total Akt levels with β-actin and subsequently used this ratio to correct p-Akt, so as to take into account total protein levels.

^{1}H-NMR spectroscopy and multivariate statistics

Mouse urine samples were prepared by mixing 200 µl of urine with 200 µl of distilled water and 200 µl of 0.1 M phosphate buffer (containing 10% D_2O/H_2O, v/v, and 0.05% sodium 3-trimethylsilyl-(2,2,3,3-$^2H_4$)-1-propionate as a chemical shift reference at δ 0.0). The mixtures were loaded into 96-well plates for high-throughput flow-injection NMR spectroscopy. Samples were prepared and measured on a spectrometer (Bruker) operating at 600.22 MHz ^{1}H frequency as detailed previously[13]. In short, a standard 1D pulse sequence (recycle delay-90°-t_1-90°-t_m-90°-acquisition) was used. Water suppression was performed by irradiating the water peak during the recycle delay (2 s) and mixing time, t_m (150 ms); t_1 was set to 3 µs. The 90° pulse length was adjusted to ≈10 µs. We acquired 128 transients at 32,000 a data point resolution for each spectrum with a 20 ppm spectral width. Free induction decays were multiplied by an exponential function corresponding to a 0.3-Hz line-broadening factor before Fourier transformation. The NMR spectra were corrected for phase and baseline. Full-resolution ^{1}H-NMR spectra were imported, and the area corresponding to the water region after water suppression (δ4.5–5.0) was discarded. The full-resolution spectra were then processed and analysed using O-PLS-DA as we had done previously[13]. In this version of discriminant analysis, class separation is maximized by using NMR data (X) to model the class matrix

(Y, with n dummy variables for n classes), through decomposition of the covariance matrix (Y^TX) into $n-1$ O-PLS components and additional orthogonal signal correction components[13]. Variance component analysis was performed as described previously[83]. ^{1}H-NMR profiling was performed in a single batch with the personnel blinded to treatment groups. The O-PLS-DA model was validated using 10,000 random permutations of the original class membership variable to explain (that is, diets, treatments or genotypes), as described previously[83].

Plasma methylamine quantification by UPLC–MS/MS

Methylamines were quantified according to our previously validated methods[29,30]: plasma samples (20 µl) were spiked with 10 µl internal standard solution ($^{13}C_3$/^{15}N-TMA, d_9-TMAO, d_4-choline, d_3-carnitine and d_9-betaine in water; 1 mg l^{-1}) and 45 µl of ethyl 2-bromoacetate solution (15 g l^{-1} ethyl 2-bromoacetate, 1% NH_4OH in acetonitrile) were added to derivatize methylamines (TMA and $^{13}C_3$/^{15}N-TMA) to their ethoxy-analogues, completed after 30 min at room temperature. Methylamines were derivatised with ethyl bromoacetate to increase sensitivity (the underivatized form elicited a low response from the mass spectrometer owing to its low molecular weight) and enhance chromatographic performance. A total of 935 µl of a protein/lipid precipitation solution (94% acetonitrile/5% water/1% formic acid) was added; samples were centrifuged for 20 min (4 °C, 20,000g) and transferred to UPLC–autosampler vials. Sample injections (10 µl loop) were performed on a Waters Acquity UPLC-Xevo TQ-S UPLC–MS/MS system equipped with an Acquity BEH HILIC (2.1 × 100 mm, 1.7 µm) chromatographic column. An isocratic elution was applied with 10 mM ammonium formate in 95:5 (v/v) acetronitrile:water for 14 min at 500 µl min^{-1} and 50 °C. Positive electrospray (ESI+) was used as the ionization source, and mass spectrometer parameters were set as follows: capillary, cone and source offset voltages at 500, 93 and 50 V, respectively; desolvation temperature at 600 °C; desolvation/cone/nebulizer gases were high-purity nitrogen at 1,000 l h^{-1}, 150 l h^{-1} and 7 bar, respectively. Collision gas was high-purity argon. The mass spectrometer was operated in multiple reaction monitoring mode. The monitored transitions were as follows: for derivatized-TMA, +146 → +118/59 m/z (23/27 V); for derivatised-$^{13}C_3$/^{15}N-TMA, +150 → +63 (27 V); for TMAO, +76 → +59/58 m/z (12/13 V); for d_9-TMAO, +85 → +68 m/z (18 V); for choline, +104 → +60/45 m/z (14/16 V); for d_4-choline, +108 → +60 m/z (15 V); for γ-butyrobetaine, +146 → +60/87 m/z (12/12 V); for carnitine, +162 → +103/60 m/z (16/14 V); for d_3-carnitine, +165 → +103 m/z (16 V); for betaine, +118 → +59/58 m/z (16/16 V); and for d_9-betaine, +127 → +68 m/z (16 V).

Kinome screen, K_d

TMA was assessed using the KdELECT screening service (DiscoveRx) as described previously[35,36]. This technique is based on a competition-binding assay that quantitatively measures the ability of a compound to compete with an immobilized, active-site-directed ligand. The assay consists of a DNA-tagged kinase, an immobilized ligand and the potent inhibitor. The ability of TMA to compete with the immobilized ligand was measured by qPCR of the DNA tag. K_d was then calculated from a duplicate 11-point dose–response curve. Kinase interaction tree plots were generated using the TREEspot Software Tool and are reprinted with permission from KINOMEscan, a division of DiscoveRx Corporation, 2015.

Kinase activity assays

The TMA IC_{50} on IRAK4 was determined using Kinexus kinase-inhibitor activity profiling service (Kinexus). Protein kinase assays (in duplicate) were performed at ambient temperature for 30 min in a final volume of 25 µl according to the following assay reaction recipe:

Component 1. A total of 5 µl of diluted active IRAK4 target (recombinant, full length, expressed by baculovirus in Sf9 insect cells with an GST tag (SignalChem Catalogue 112-10G); ~10–50 nM final concentration in the assay).

Component 2. A total of 5 µl of stock solution of substrate (Myelin Basic Protein 1 mg ml^{-1} diluted in H_2O).

Component 3. A total of 5 µl of kinase assay buffer (25 mM MOPS pH 7.2, 12.5 mM β-glycerol-phosphate, 25 mM $MgCl_2$, 5 mM EGTA, 2 mM EDTA, 0.25 mM dithiothreitol, added just before assay initiation).

Component 4. A total of 5 µl of compound (various concentrations as indicated) or 10% dimethylsulfoxide for blank.

Component 5. A total of 5 µl of ^{32}P-ATP (250 µM stock solution, 0.8 µCi, Perkin Elmer).

The assay was initiated by the addition of ^{32}P-ATP, and the reaction mixture was incubated at ambient temperature for 30 min. After the incubation period, the assay was terminated by spotting 10 µl of the reaction mixture onto a Multiscreen phosphocellulose P81 plate, which was washed three times, each time for approximately 15 min, in a 1% phosphoric acid solution. The radioactivity on the P81 plate was counted in the presence of scintillation fluid in a Trilux scintillation counter. Blank control was set up that included all the assay components except the addition of Myelin Basic Protein (replaced with an equal volume of assay dilution buffer). The corrected activity for the IRAK4 target was determined by removing the blank control value.

We calculated the TMA K_i for IRAK4 using the equation below[84], where IC_{50} = 3.4 µM, as determined from the IRAK4 activity assay described above. [S] is the concentration of ATP in the assay (50 µM), and the K_m value of IRAK4 for ATP (K_m = 13.6 µM) was provided by the commercial vendor. Purified IRAK4 for these assays was obtained from https://media.cellsignal.com/pdf/7551.pdf.

$$K_i = \frac{IC_{50}}{1 + \frac{[S]}{K_m}}$$

Reagents

Glutamine (Glutamax, 35050061, Life Technologies), FBS (Life Technologies), crystal violet (C6158) and trimethylamine solution (W324108) were obtained from Sigma-Aldrich. Mouse IL-6 Quantikine ELISA kits (M6000B) were obtained from R&D Systems, and the RNeasy Micro Kit was from Qiagen. SuperScript II Reverse Transcriptase, IL-6 Taqman probe Hs00174131_m1 and FAST master mix were purchased from Invitrogen. The HFD (Special Diets Services) and CHD (B&K Universal) were specifically formulated as described in a previous publication[12]; the remaining foods were obtained from Research Diets: control diet (D12450K), LC-HFD (60% kcal fat and 20% kcal carbohydrates; D12492), and HC-HFD (60% kcal fat and 20% kcal carbohydrates with 17 g of choline per kg; D16100401i). The mouse insulin ELISA was obtained from Mercodia (10-1249-01). Additional reagents and kits included isoflurane (10014451, Forene, Abbott); TriPure reagent (1667165, Roche); Reverse Transcription System kit (A3500, Promega); Mesa Fast qPCR (CS-CKIT-PROD, Eurogentec); and the MSD V-PLEX Plus Proinflammatory Panel 1 kit (K15048G Meso Scale Diagnostics).

Statistics

Potential outliers were identified by a Grubbs test. For statistical comparisons between study groups, normality was tested using the D'agostino–Pearson omnibus normality test, then one-way ANOVA was used, followed by Tukey's post hoc testing when data were normally distributed; otherwise, groups were compared using the two-tailed Mann–Whitney test ($P < 0.05$ considered to be statistically significant). Where applicable, P values were corrected for multiple comparisons using the Benjamini–Hochberg method, unless otherwise stated. Data are displayed as means ± s.e.m in all figures. All cell culture

experiments included at least three biological replicates (as indicated in figure legends). All animal cohorts included at least five animals in each study group (as indicated in figure legends); animals were randomized to treatment groups and were sampled in a random order. Data collection and analysis were not performed blind to the conditions of the experiments. No statistical methods were used to pre-determine sample sizes, but our sample sizes are similar to those reported in our previous publications[69].

Reporting summary

Further information on research design is available in the Nature Portfolio Reporting Summary linked to this article.

Data availability

Microarray data are deposited in ArrayExpress under accession number E-MEXP-1755. ^{1}H-NMR-based metabolomics data are deposited in Metabolights with accession number MTBLS12989 (https://www.ebi.ac.uk/metabolights/MTBLS12989). The UPLC–MS/MS spectra for isotopically quantified methylamines are deposited in Metabolights with accession number MTBLS12975 (https://www.ebi.ac.uk/metabolights/MTBLS12975). Source data are provided with this paper.

Code availability

No custom code or algorithm was used for the analyses conducted in this work.

References

1. Ong, K. L. et al. Global, regional, and national burden of diabetes from 1990 to 2021, with projections of prevalence to 2050: a systematic analysis for the Global Burden of Disease Study 2021. *Lancet* **402**, 203–234 (2023).
2. Samuel, V. T. & Shulman, G. I. Mechanisms for insulin resistance: common threads and missing links. *Cell* **148**, 852–871 (2012).
3. Cai, D. et al. Local and systemic insulin resistance resulting from hepatic activation of IKK-β and NF-κB. *Nat. Med.* **11**, 183–190 (2005).
4. Wu, G. D. et al. Linking long-term dietary patterns with gut microbial enterotypes. *Science* **334**, 105–108 (2011).
5. Le Chatelier, E. et al. Richness of human gut microbiome correlates with metabolic markers. *Nature* **500**, 541–546 (2013).
6. Pedersen, H. K. et al. Human gut microbes impact host serum metabolome and insulin sensitivity. *Nature* **535**, 376–381 (2016).
7. Cani, P. D. et al. Metabolic endotoxemia initiates obesity and insulin resistance. *Diabetes* **56**, 1761–1772 (2007).
8. Hooper, L. V., Littman, D. R. & Macpherson, A. J. Interactions between the microbiota and the immune system. *Science* **336**, 1268–1273 (2012).
9. Nicholson, J. K. et al. Host–gut microbiota metabolic interactions. *Science* **336**, 1262–1267 (2012).
10. Maslowski, K. M. et al. Regulation of inflammatory responses by gut microbiota and chemoattractant receptor GPR43. *Nature* **461**, 1282–1286 (2009).
11. Venkatesh, M. et al. Symbiotic bacterial metabolites regulate gastrointestinal barrier function via the xenobiotic sensor PXR and Toll-like receptor 4. *Immunity* **41**, 296–310 (2014).
12. Manning, G., Whyte, D. B., Martinez, R., Hunter, T. & Sudarsanam, S. The protein kinase complement of the human genome. *Science* **298**, 1912–1934 (2002).
13. Dumas, M.-E. et al. Metabolic profiling reveals a contribution of gut microbiota to fatty liver phenotype in insulin-resistant mice. *Proc. Natl Acad. Sci. USA* **103**, 12511–12516 (2006).
14. Wang, Z. et al. Gut flora metabolism of phosphatidylcholine promotes cardiovascular disease. *Nature* **472**, 57–63 (2011).
15. Al-Waiz, M., Mikov, M., Mitchell, S. C. & Smith, R. L. The exogenous origin of trimethylamine in the mouse. *Metabolism* **41**, 135–136 (1992).
16. Craciun, S. & Balskus, E. P. Microbial conversion of choline to trimethylamine requires a glycyl radical enzyme. *Proc. Natl Acad. Sci. USA* **109**, 21307–21312 (2012).
17. Koeth, R. A. et al. Intestinal microbiota metabolism of l-carnitine, a nutrient in red meat, promotes atherosclerosis. *Nat. Med.* **19**, 576–585 (2013).
18. Al-Waiz, M., Ayesh, R., Mitchell, S. C., Idle, J. R. & Smith, R. L. Disclosure of the metabolic retroversion of trimethylamine *N*-oxide in humans: a pharmacogenetic approach. *Clin. Pharmacol. Ther.* **42**, 608–612 (1987).
19. Hoyles, L. et al. Metabolic retroconversion of trimethylamine *N*-oxide and the gut microbiota. *Microbiome* **6**, 73 (2018).
20. Dolphin, C. T., Janmohamed, A., Smith, R. L., Shephard, E. A. & Phillips, L. R. Missense mutation in flavin-containing mono-oxygenase 3 gene, *FMO3*, underlies fish-odour syndrome. *Nat. Genet.* **17**, 491–494 (1997).
21. Shih, D. M. et al. Flavin containing monooxygenase 3 exerts broad effects on glucose and lipid metabolism and atherosclerosis. *J. Lipid Res.* **56**, 22–37 (2015).
22. Warrier, M. et al. The TMAO-generating enzyme flavin monooxygenase 3 is a central regulator of cholesterol balance. *Cell Rep.* **10**, 326–338 (2015).
23. Miao, J. et al. Flavin-containing monooxygenase 3 as a potential player in diabetes-associated atherosclerosis. *Nat. Commun.* **6**, 6498 (2015).
24. Schugar, R. C. et al. The TMAO-producing enzyme flavin-containing monooxygenase 3 regulates obesity and the beiging of white adipose tissue. *Cell Rep.* **19**, 2451–2461 (2017).
25. Özcan, U. et al. Endoplasmic reticulum stress links obesity, insulin action, and type 2 diabetes. *Science* **306**, 457–461 (2004).
26. Eckel-Mahan, K. L. et al. Reprogramming of the circadian clock by nutritional challenge. *Cell* **155**, 1464–1478 (2013).
27. Thorens, B. et al. Use of preclinical models to identify markers of type 2 diabetes susceptibility and novel regulators of insulin secretion—a step towards precision medicine. *Mol. Metab.* **27**, S147–S154 (2019).
28. Dumas, M.-E. et al. Microbial-host co-metabolites are prodromal markers predicting phenotypic heterogeneity in behavior, obesity, and impaired glucose tolerance. *Cell Rep.* **20**, 136–148 (2017).
29. Fromentin, S. et al. Microbiome and metabolome features of the cardiometabolic disease spectrum. *Nat. Med.* **28**, 303–314 (2022).
30. Forslund, S. K. et al. Combinatorial, additive and dose-dependent drug–microbiome associations. *Nature* **600**, 500–505 (2021).
31. Matsuda, M. & DeFronzo, R. A. Insulin sensitivity indices obtained from oral glucose tolerance testing: comparison with the euglycemic insulin clamp. *Diabetes Care* **22**, 1462–1470 (1999).
32. Liu, H.-Y. et al. Increased basal level of Akt-dependent insulin signaling may be responsible for the development of insulin resistance. *Am. J. Physiol. Endocrinol. Metab.* **297**, E898–E906 (2009).
33. Sack, G. H. Serum amyloid A—a review. *Mol. Med.* **24**, 46 (2018).
34. Wang, Z. et al. Non-lethal inhibition of gut microbial trimethylamine production for the treatment of atherosclerosis. *Cell* **163**, 1585–1595 (2015).
35. Fabian, M. A. et al. A small molecule–kinase interaction map for clinical kinase inhibitors. *Nat. Biotechnol.* **23**, 329–336 (2005).
36. Karaman, M. W. et al. A quantitative analysis of kinase inhibitor selectivity. *Nat. Biotechnol.* **26**, 127–132 (2008).
37. Sun, X.-J. et al. Deletion of interleukin 1 receptor-associated kinase 1 (*Irak1*) improves glucose tolerance primarily by increasing insulin sensitivity in skeletal muscle. *J. Biol. Chem.* **292**, 12339–12350 (2017).

38. Suzuki, N. et al. Severe impairment of interleukin-1 and Toll-like receptor signalling in mice lacking IRAK-4. *Nature* **416**, 750–754 (2002).
39. Picard, C. et al. Pyogenic bacterial infections in humans with IRAK-4 deficiency. *Science* **299**, 2076–2079 (2003).
40. Lee, K. L. et al. Discovery of clinical candidate 1-{[(2 *S*, 3 *S*, 4 *S*)-3-Ethyl-4-fluoro-5-oxopyrrolidin-2-yl]methoxy}-7-methoxyisoquinoline-6-carboxamide (PF-06650833), a potent, selective inhibitor of interleukin-1 receptor associated kinase 4 (IRAK4), by fragment-based drug design. *J. Med. Chem.* **60**, 5521–5542 (2017).
41. Ku, C.-L. et al. Selective predisposition to bacterial infections in IRAK-4–deficient children: IRAK-4-dependent TLRs are otherwise redundant in protective immunity. *J. Exp. Med.* **204**, 2407–2422 (2007).
42. Kollewe, C. et al. Sequential autophosphorylation steps in the interleukin-1 receptor-associated kinase-1 regulate its availability as an adapter in interleukin-1 signaling. *J. Biol. Chem.* **279**, 5227–5236 (2004).
43. Kim, T. W. et al. A critical role for IRAK4 kinase activity in Toll-like receptor-mediated innate immunity. *J. Exp. Med.* **204**, 1025–1036 (2007).
44. Hoyles, L. et al. Molecular phenomics and metagenomics of hepatic steatosis in non-diabetic obese women. *Nat. Med.* **24**, 1070–1080 (2018).
45. Valaperti, A. et al. Innate immune interleukin-1 receptor-associated kinase 4 exacerbates viral myocarditis by reducing $CCR5^+$ $CD11b^+$ monocyte migration and impairing interferon production. *Circulation* **128**, 1542–1554 (2013).
46. Winkler, A. et al. The interleukin-1 receptor-associated kinase 4 inhibitor PF-06650833 blocks inflammation in preclinical models of rheumatic disease and in humans enrolled in a randomized clinical trial. *Arthritis Rheumatol.* **73**, 2206–2218 (2021).
47. O'Neill, L. A. J., Golenbock, D. & Bowie, A. G. The history of Toll-like receptors—redefining innate immunity. *Nat. Rev. Immunol.* **13**, 453–460 (2013).
48. von Bernuth, H., Picard, C., Puel, A. & Casanova, J.-L. Experimental and natural infections in MyD88- and IRAK-4-deficient mice and humans. *Eur. J. Immunol.* **42**, 3126–3135 (2012).
49. Caesar, R., Tremaroli, V., Kovatcheva-Datchary, P., Cani, P. D. & Bäckhed, F. Crosstalk between gut microbiota and dietary lipids aggravates WAT inflammation through TLR signaling. *Cell Metab.* **22**, 658–668 (2015).
50. Shi, H. et al. TLR4 links innate immunity and fatty acid–induced insulin resistance. *J. Clin. Invest.* **116**, 3015–3025 (2006).
51. Reilly, S. M. et al. An inhibitor of the protein kinases TBK1 and IKK-ε improves obesity-related metabolic dysfunctions in mice. *Nat. Med.* **19**, 313–321 (2013).
52. Kiechl, S. et al. Blockade of receptor activator of nuclear factor-κB (RANKL) signaling improves hepatic insulin resistance and prevents development of diabetes mellitus. *Nat. Med.* **19**, 358–363 (2013).
53. Bain, M. A., Faull, R., Fornasini, G., Milne, R. W. & Evans, A. M. Accumulation of trimethylamine and trimethylamine-*N*-oxide in end-stage renal disease patients undergoing haemodialysis. *Nephrol. Dial. Transplant.* **21**, 1300–1304 (2006).
54. Lundh, T., Akesson, B. & Skerfving, S. Effect of dietary intake of trimethylamine on human metabolism of the industrial catalyst dimethylethylamine. *Occup. Environ. Med.* **52**, 478–483 (1995).
55. Dumas, M.-E. The microbial–mammalian metabolic axis: beyond simple metabolism. *Cell Metab.* **13**, 489–490 (2011).
56. Spencer, M. D. et al. Association between composition of the human gastrointestinal microbiome and development of fatty liver with choline deficiency. *Gastroenterology* **140**, 976–986 (2011).
57. Gao, X., Wang, Y. & Sun, G. High dietary choline and betaine intake is associated with low insulin resistance in the Newfoundland population. *Nutrition* **33**, 28–34 (2017).
58. Everard, A. et al. Intestinal epithelial MyD88 is a sensor switching host metabolism towards obesity according to nutritional status. *Nat. Commun.* **5**, 5648 (2014).
59. Andrikopoulos, P. et al. Evidence of a causal and modifiable relationship between kidney function and circulating trimethylamine *N*-oxide. *Nat. Commun.* **14**, 5843 (2023).
60. Hoyles, L. et al. Regulation of blood–brain barrier integrity by microbiome-associated methylamines and cognition by trimethylamine *N*-oxide. *Microbiome* **9**, 235 (2021).
61. Chou, R.-H. et al. Paradox of trimethylamine-*N*-oxide, the impact of malnutrition on microbiota-derived metabolites and septic patients. *J. Intensive Care* **9**, 65 (2021).
62. Meyer, K. A. et al. Microbiota-dependent metabolite trimethylamine *N*-oxide and coronary artery calcium in the Coronary Artery Risk Development in Young Adults Study (CARDIA). *J. Am. Heart Assoc.* **5**, e003970 (2016).
63. Yao, M.-E., Liao, P.-D., Zhao, X.-J. & Wang, L. Trimethylamine-*N*-oxide has prognostic value in coronary heart disease: a meta-analysis and dose–response analysis. *BMC Cardiovasc. Disord.* **20**, 7 (2020).
64. Papandreou, C. et al. Plasma trimethylamine-*N*-oxide and related metabolites are associated with type 2 diabetes risk in the Prevención con Dieta Mediterránea (PREDIMED) trial. *Am. J. Clin. Nutr.* **108**, 163–173 (2018).
65. Li, S. et al. Serum trimethylamine-*N*-oxide is associated with incident type 2 diabetes in middle-aged and older adults: a prospective cohort study. *J. Transl. Med.* **20**, 374 (2022).
66. Svingen, G. F. T. et al. Prospective associations of systemic and urinary choline metabolites with incident type 2 diabetes. *Clin. Chem.* **62**, 755–765 (2016).
67. Roy, S., Yuzefpolskaya, M., Nandakumar, R., Colombo, P. C. & Demmer, R. T. Plasma trimethylamine-*N*-oxide and impaired glucose regulation: results from The Oral Infections, Glucose Intolerance and Insulin Resistance Study (ORIGINS). *PLoS ONE* **15**, e0227482 (2020).
68. Kong, L. et al. Trimethylamine *N*-oxide impairs β-cell function and glucose tolerance. *Nat. Commun.* **15**, 2526 (2024).
69. Brial, F. et al. Human and preclinical studies of the host–gut microbiome co-metabolite hippurate as a marker and mediator of metabolic health. *Gut* **70**, 2105–2114 (2021).
70. Jaworska, K., Bielinska, K., Gawrys-Kopczynska, M. & Ufnal, M. TMA (trimethylamine), but not its oxide TMAO (trimethylamine-oxide), exerts haemodynamic effects: implications for interpretation of cardiovascular actions of gut microbiome. *Cardiovasc. Res.* **115**, 1948–1949 (2019).
71. Chen, S. et al. Trimethylamine *N*-oxide binds and activates PERK to promote metabolic dysfunction. *Cell Metab.* **30**, 1141–1151.e5 (2019).
72. Laakso, M. & Kuusisto, J. Insulin resistance and hyperglycaemia in cardiovascular disease development. *Nat. Rev. Endocrinol.* **10**, 293–302 (2014).
73. Ahmetaj-Shala, B. et al. A bioassay system of autologous human endothelial, smooth muscle cells, and leukocytes for use in drug discovery, phenotyping, and tissue engineering. *FASEB J.* **34**, 1745–1754 (2020).
74. Latorre, J. et al. Decreased lipid metabolism but increased FA biosynthesis are coupled with changes in liver microRNAs in obese subjects with NAFLD. *Int. J. Obes.* **41**, 620–630 (2017).
75. Toye, A. A. et al. Subtle metabolic and liver gene transcriptional changes underlie diet-induced fatty liver susceptibility in insulin-resistant mice. *Diabetologia* **50**, 1867–1879 (2007).

76. Geurts, L., Muccioli, G. G., Delzenne, N. M. & Cani, P. D. Chronic endocannabinoid system stimulation induces muscle macrophage and lipid accumulation in type 2 diabetic mice independently of metabolic endotoxaemia. *PLoS ONE* **8**, e55963 (2013).
77. Gentleman, R., Carey, V. J., Huber, W., Irizarry, R. A. & Dudoit, S. (eds) *Bioinformatics and Computational Biology Solutions Using R and Bioconductor* (Springer, 2005).
78. Smyth, G. K. limma: linear models for microarray data. In *Bioinformatics and Computational Biology Solutions Using R and Bioconductor* (eds Gentleman, R. et al.) 397–420 (Springer-Verlag, 2005).
79. Chen, E. Y. et al. Enrichr: interactive and collaborative HTML5 gene list enrichment analysis tool. *BMC Bioinformatics* **14**, 128 (2013).
80. Tarca, A. L. et al. A novel signaling pathway impact analysis. *Bioinformatics* **25**, 75–82 (2009).
81. Lee, J.-M. et al. Serum amyloid A3 exacerbates cancer by enhancing the suppressive capacity of myeloid-derived suppressor cells via TLR2-dependent STAT3 activation: cellular immune response. *Eur. J. Immunol.* **44**, 1672–1684 (2014).
82. Plovier, H. et al. A purified membrane protein from *Akkermansia muciniphila* or the pasteurized bacterium improves metabolism in obese and diabetic mice. *Nat. Med.* **23**, 107–113 (2017).
83. Blaise, B. J. et al. Metabotyping of *Caenorhabditis elegans* reveals latent phenotypes. *Proc. Natl Acad. Sci. USA* **104**, 19808–19812 (2007).
84. Cheng, Y. & Prusoff, W. H. Relationship between the inhibition constant (K1) and the concentration of inhibitor which causes 50 per cent inhibition (I50) of an enzymatic reaction. *Biochem. Pharmacol.* **22**, 3099–3108 (1973).

Acknowledgements

This work was supported by grants from the Wellcome Trust (Functional Genomics Initiative grant Biological Atlas of Insulin Resistance 06678 to J.K.N., D.G. and J.S.) and the European Commission (METACARDIS HEALTH-F4-2012-305312 to D.G. and M.E.D.), Institut Mérieux through a grant awarded to M.E.D., Spanish Institute of Health Research (FIS) grant (PI18/01022, PI21/01361 and PI24/00185), by Fondo Europeo de Desarrollo Regional (FEDER) funds, the Catalan Government (AGAUR, #SGR2017-00734, ICREA Academia Award 2021) to J.M.F.R. and Canadian Institutes of Health Research (CIHR) grants (MOP-49413 and MOP-142471) awarded to P.P.L. M.F. acknowledges support from MUR-PNRR M4C2I1.3 PE6 project PE00000019 Heal Italia, DARE–DigitAl lifelong pRevEntion initiative PNC0000002 and PNRR-MAD-2022-12376543 ATHEROMICS. P.L. is supported in part by Brain-Heart Interconnectome CFREF grant (Federal Government of Canada); Government of Canada through Genome Canada and Ontario Genomics (OGI-2050); and Brain Canada Foundation / Heart and Stroke Foundation of Canada for Heart-Brain Connection IMPACT Award. D.S. was a recipient of a Heart and Stroke Foundation of Canada research fellowship. The laboratory of M.E.D. has received funding from the UK Medical Research Council (MRC grants MR/M501797/1, MR/ X010155/1 and 'National Mouse Genetics Network Microbiome Cluster' MR/W022532/1), and by grants from the French National Research Agency (ANR-25-CE14-1815-01 and ANR-10-LABX-46, European Genomics Institute for Diabetes), from the National Center for Precision Diabetic Medicine–PreciDIAB, which is jointly supported by the French National Agency for Research (ANR-18-IBHU-0001), by the European Union (FEDER), by the Hauts-de-France Regional Council (Agreement 20001891/NP0025517), by the European Metropolis of Lille (MEL, Agreement 2019_ESR_11) and by Isite ULNE (R-002-20-TALENT-DUMAS), also jointly funded by ANR (ANR-16-IDEX-0004-ULNE), the Hauts-de-France Regional Council (20002845) and by the European Metropolis of Lille (MEL) and by an ERC Generator Grant 'Richness' (R-ERCGEN-23-003-DUMAS) from the University of Lille. This research was also supported by the National Institute for Health Research (NIHR) Imperial Biomedical Research Centre (M.E.D., S.D.G., M.T.). D.G. held a Wellcome Trust Senior Fellowship in Basic Biomedical Science (057733). D.G. acknowledges financial support from the INSERM International Research Project DIABETOMARKERS. J.E.F. was supported by the Medical Research Council (grant number MR/K020919/1). B.A.-S. is funded by a British Heart Foundation Fellowship RE/18/4/34215, The Rosetrees Trust project grant PGL22/100085 and MRC New Investigator Research Grant MR/Y001028/1. P.A. is the recipient of a Career Development Award from the Medical Research Council (Grant No. MR/Y010051/1). L.H. received an MRC Intermediate Research Fellowship in Data Science (grant number MR/L01632X/1, UK Med-Bio). A.E. is a research associate from the FRS-FNRS (Fonds de la Recherche Scientifique) and recipient of grants from FNRS and FRFS-WELBIO (grant no. T.0115.24 and FNRS FRFS-WELBIO under grant no. WELBIO X.1517.24). P.D.C. is an honorary research director at FRS-FNRS and is a recipient of grants from FRFS-WELBIO: WELBIO-CR-2022A-02P, EOS: program no. 40007505.

Author contributions

J.C., P.A., B.A.S. and S.G. performed cell-based assays. J.C. performed multivariate statistics and interpreted the results. J.C., F.B., J.F.F., A.E., H.P., L.Z., D.S., A.R.R., P.D.C., V.C., R.M., S.C. and C.G. contributed to the in vivo experiments. R.H.B., A.M., A.L.N., L.M.G., S.G., J.M.M.N., J.L., C.L.B. and S.P. performed various experiments. L.H. analysed microarray data. J.S., D.G., J.K.N., P.P.L., P.D.C., J.M.F.R., N.J.G. and M.E.D. conceived the project, mentored and supervised its participants and interpreted its results. M.E.D. performed metabolic profiling experiments, analysed data and interpreted the results. J.C., P.A., N.J.G., D.G., P.P.L., P.D.C. and M.E.D. wrote the manuscript. All authors edited and approved the manuscript.

Competing interests

A.E. and P.D.C. are inventors on patent applications dealing with the use of *Akkermansia muciniphila* and its components in the treatment of metabolic disorders. A.E. and P.D.C. are inventors on patent applications dealing with gut microbes in food reward dysregulations. M.E.D. is inventor on patent applications related to microbial metabolites in obesity. A.E. is an inventor on patent applications dealing with the use of bacterial metabolites in the prevention or treatment of respiratory viral infections. P.D.C. was the cofounder of Enterosys. All other authors declare no competing interests.

Additional information

Extended data is available for this paper at https://doi.org/10.1038/s42255-025-01413-8.

Supplementary information The online version contains supplementary material available at https://doi.org/10.1038/s42255-025-01413-8.

Correspondence and requests for materials should be addressed to Marc-Emmanuel Dumas.

Peer review information *Nature Metabolism* thanks Markus Seeliger and the other, anonymous, reviewer(s) for their contribution to the peer review of this work. Primary Handling Editor: Yanina-Yasmin Pesch, in collaboration with the *Nature Metabolism* team.

Reprints and permissions information is available at www.nature.com/reprints.

Publisher's note Springer Nature remains neutral with regard to jurisdictional claims in published maps and institutional affiliations.

Open Access This article is licensed under a Creative Commons Attribution 4.0 International License, which permits use, sharing, adaptation, distribution and reproduction in any medium or format, as long as you give appropriate credit to the original author(s) and the source, provide a link to the Creative Commons licence, and indicate if changes were made. The images or other third party material in this article are included in the article's Creative Commons licence, unless indicated otherwise in a credit line to the material. If material is not included in the article's Creative Commons licence and your intended use is not permitted by statutory regulation or exceeds the permitted use, you will need to obtain permission directly from the copyright holder. To view a copy of this licence, visit http://creativecommons.org/licenses/by/4.0/.

© The Author(s) 2025

Julien Chilloux[1,22], Francois Brial[2,22], Amandine Everard[3,4,22], David Smyth[5,22], Petros Andrikopoulos[1,22], Liyong Zhang[5], Hubert Plovier[3,4], Antonis Myridakis[1], Lesley Hoyles[1,6], José Maria Moreno-Navarrete[7,8,9], Jèssica Latorre Luque[7,8,9], Viviana Casagrande[10], Rossella Menghini[10], Blerina Ahmetaj-Shala[11], Christine Blancher[12], Laura Martinez-Gili[1], Selin Gencer[1], Jane F. Fearnside[12], Richard H. Barton[1,23], Ana Luisa Neves[1], Alice R. Rothwell[12], Christelle Gérard[13], Sophie Calderari[14], Mark J. Williamson[15], Julian E. Fuchs[15], Lata Govada[1], Claire L. Boulangé[1], Saroor Patel[1], James Scott[15], Mark Thursz[16], Naomi Chayen[1], Robert C. Glen[1,15], Nigel J. Gooderham[1], Jeremy K. Nicholson[1,17], Massimo Federici[10], José Manuel Fernández-Real[7,8,9,18], Dominique Gauguier[12,13,19,24], Peter P. Liu[5,24], Patrice D. Cani[1,3,4,20,24] & Marc-Emmanuel Dumas[1,19,21,24] ✉

[1]Section of Biomolecular Medicine, Division of Systems Medicine, Department of Metabolism, Digestion and Reproduction, Imperial College London, London, UK. [2]University Paris Cité, INSERM U1132, Biologie de l'os et du cartilage (BIOSCAR), Paris, France. [3]Université catholique de Louvain, Louvain Drug Research Institute, Metabolism and Nutrition Research Group, Brussels, Belgium. [4]Walloon Excellence in Life Sciences and Biotechnology (WELBIO) Department, WEL Research Institute, Wavre, Belgium. [5]University of Ottawa Heart Institute, Ottawa, Ontario, Canada. [6]Department of Biosciences, Nottingham Trent University, Clifton Campus, Nottingham, UK. [7]Department of Endocrinology, Diabetes and Nutrition, University Hospital of Girona 'Dr Josep Trueta', Girona, Spain. [8]Institut d'Investigació Biomèdica de Girona (IdibGi), Girona, Spain. [9]CIBER Fisiopatología de la Obesidad y Nutrición (CIBERobn), Instituto de Salud Carlos III, Madrid, Spain. [10]Department of Systems Medicine, University of Rome Tor Vergata, Via Montpellier, Rome, Italy. [11]Section of Cardio-Respiratory Interface, National Heart & Lung Institute, Imperial College London, London, UK. [12]Wellcome Trust Centre for Human Genetics, Roosevelt Drive, University of Oxford, Oxford, UK. [13]University Paris Cité, Functional and Adaptive Biology, CNRS UMR 8251, Paris, France. [14]University Paris-Saclay, INRAE, Jouy-en-Josas, France. [15]Centre for Molecular Informatics, Department of Chemistry, University of Cambridge, Cambridge, UK. [16]Section of Hepatology & Gastroenterology, Division of Digestive Diseases, Department of Metabolism, Digestion and Reproduction, Imperial College London, London, UK. [17]The Australian National Phenome Centre, Health Futures Institute, Murdoch University, Harry Perkins Institute, Perth, Australia. [18]Department of Medical Sciences, School of Medicine, University of Girona, Girona, Spain. [19]Victor Phillip Dahdaleh Institute of Genomic Medicine at McGill University, Montreal, Quebec, Canada. [20]Institute of Experimental and Clinical Research (IREC), UCLouvain, Université catholique de Louvain, Brussels, Belgium. [21]European Genomic Institute for Diabetes, U1283 INSERM, UMR8199 CNRS, Institut Pasteur de Lille, Lille University Hospital, University of Lille, Lille, France. [22]These authors contributed equally: Julien Chilloux, Francois Brial, Amandine Everard, David Smyth, Petros Andrikopoulos. [23]Deceased: Richard H. Barton. [24]These authors jointly supervised this work: Dominique Gauguier, Peter P. Liu, Patrice D. Cani, Marc-Emmanuel Dumas. ✉e-mail: m.dumas@imperial.ac.uk

https://doi.org/10.1038/s42255-025-01413-8

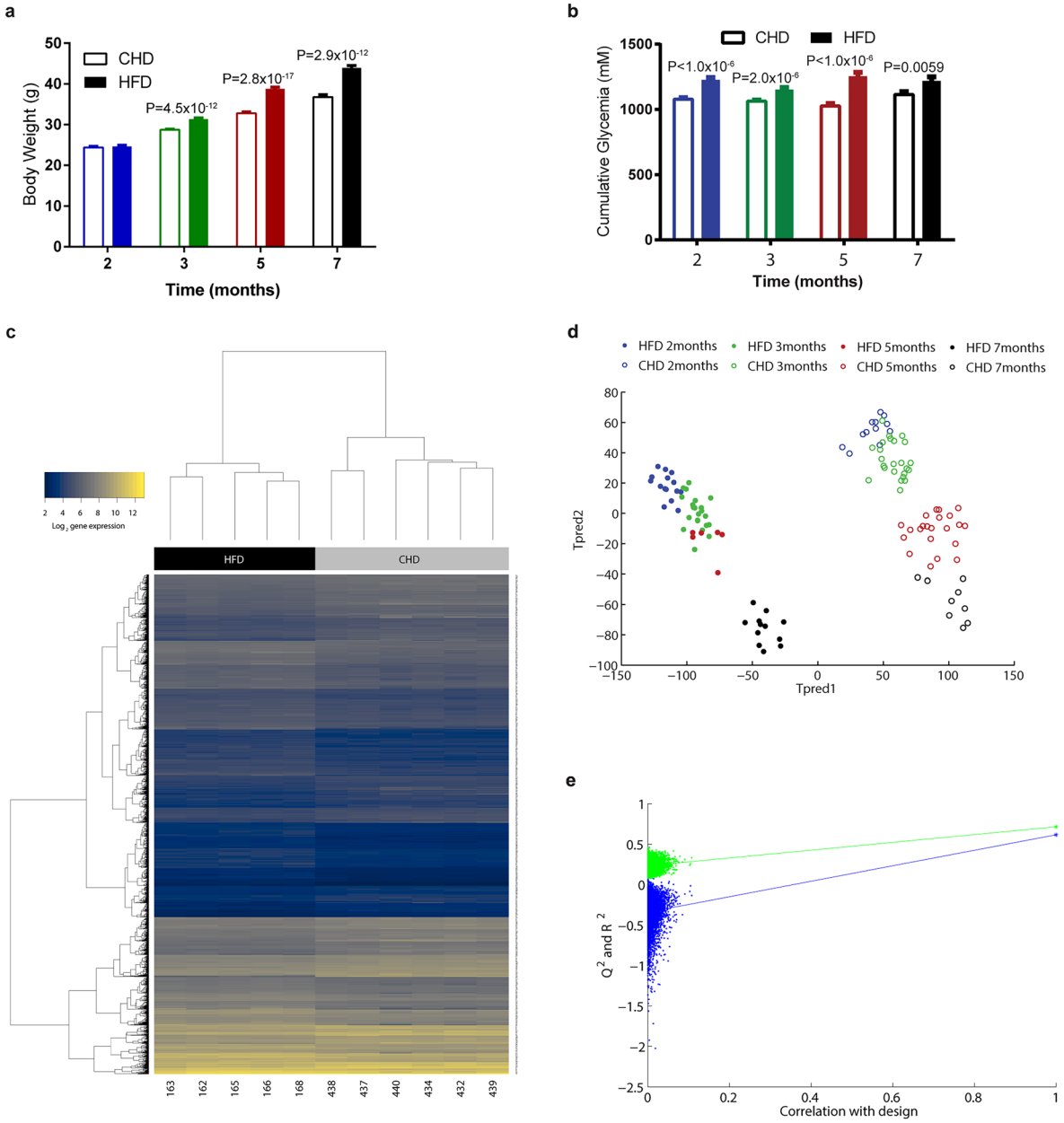

Extended Data Fig. 1 | C57BL/6 mice fed HFD display low acute-phase gene expression in liver paralleled by high TMA excretion. Male mice were weaned at 3 weeks and fed CHD, before being randomly assigned to CHD group (n = 270) or HFD (n = 202) groups and monitored at 2 (72 CHD and 64 HFD), 3 (84 CHD and 57 HFD), 5 (68 CHD and 47 HFD) and 7 months (46 CHD and 34 HFD). (**a**, **b**) Effect of HFD-feeding on physiological parameters. (**a**) Body weight (BW) and (**b**) cumulative glycemia during GTT (AUC). (**c**) Heatmap of significantly (FDR < 0.1) differentially expressed liver genes after 4 months of HFD. (**d**) ^{1}H-NMR-based metabotyping scores plot from a cross-validated O-PLS-DA model segregating the eight groups of mice according to both diet and age. (**e**) Empirical assessment of the significance of O-PLS goodness-of-fit parameters by generating a null distribution with 10,000 random permutations. Data are means ± s.e.m. Two-sided Mann-Whitney test (*$P < 0.05$ vs control). For the O-PLS-DA permutation test, the horizontal axis corresponds to the correlation between the original class membership variable (single dots on the right) and the randomly permuted class membership vectors (no longer correlated with the original class membership) (swarm of permutated models on the left). The *y* axis corresponds to goodness-of-fit parameter R^2 (in green) derived for each O-PLS-DA model and the goodness-of-prediction parameter Q^2 (in blue) derived by 7-fold cross-validation of each O-PLS-DA model. The R^2 and Q^2 parameters obtained from the original model in the top right corner are outside the confidence interval of the 10,000 randomly permuted models and therefore confirming the significance of the fitness and prediction capacity of the original O-PLS-DA model. Source data are provided.

https://doi.org/10.1038/s42255-025-01413-8

a

SIGNIFICANTLY DOWNREGULATED GENES

Biological Process	Combined Score	FDR	Overlap
organic acid catabolic process (GO:0016054)	41.00	1.50499E-08	35/200
carboxylic acid catabolic process (GO:0046395)	40.95	1.50499E-08	35/200
cellular amino acid metabolic process (GO:0006520)	40.58	3.70459E-08	51/421
small molecule catabolic process (GO:0044282)	40.28	3.70459E-08	39/261
dicarboxylic acid metabolic process (GO:0043648)	35.76	1.28014E-07	22/87
coenzyme metabolic process (GO:0006732)	29.63	2.15627E-06	30/196
alpha-amino acid catabolic process (GO:1901606)	29.56	1.35749E-06	21/92
cofactor metabolic process (GO:0051186)	28.76	3.83676E-06	34/255
cellular amino acid catabolic process (GO:0009063)	28.58	2.15627E-06	23/117
alpha-amino acid metabolic process (GO:1901605)	23.67	2.84938E-05	29/213

Cellular Component	Combined Score	FDR	Overlap
organelle inner membrane (GO:0019866)	41.00	3.44957E-08	46/360
mitochondrial membrane (GO:0031966)	39.91	4.49838E-08	52/457
mitochondrial inner membrane (GO:0005743)	38.28	7.03569E-08	43/341
mitochondrion (GO:0005739)	20.34	0.00014029	88/1269
extracellular vesicular exosome (GO:0070062)	16.15	0.000578346	155/2717
very-low-density lipoprotein particle (GO:0034361)	9.70	0.015960442	6/20
oxidoreductase complex (GO:1990204)	9.67	0.010057058	13/88
triglyceride-rich lipoprotein particle (GO:0034385)	9.41	0.015960442	6/20
plasma lipoprotein particle (GO:0034358)	9.36	0.015960442	8/38
mitochondrial matrix (GO:0005759)	9.30	0.015158891	21/208

Molecular Function	Combined Score	FDR	Overlap
cofactor binding (GO:0048037)	33.40	1.50742E-06	36/266
pyridoxal phosphate binding (GO:0030170)	15.98	0.000932731	13/57
lyase activity (GO:0016829)	12.48	0.005557205	21/177
coenzyme binding (GO:0050662)	12.35	0.005557205	22/188
carbon-nitrogen lyase activity (GO:0016840)	9.28	0.022905778	5/10
NADH dehydrogenase (quinone) activity (GO:0050136)	8.95	0.022905778	9/46
NADH dehydrogenase (ubiquinone) activity (GO:0008137)	8.87	0.022905778	9/46
NADH dehydrogenase activity (GO:0003954)	8.78	0.022905778	9/46
lysophosphatidic acid acyltransferase activity (GO:0042171)	8.22	0.030487068	5/12
flavin adenine dinucleotide binding (GO:0050660)	7.59	0.032683964	11/74

SIGNIFICANTLY UPREGULATED GENES

Biological Process	Combined Score	FDR	Overlap
response to endoplasmic reticulum stress (GO:0034976)	63.79	5.5045E-13	39/145
ER-nucleus signaling pathway (GO:0006984)	50.43	1.22345E-10	29/94
endoplasmic reticulum unfolded protein response (GO:0030968)	49.22	2.10104E-10	27/83
response to unfolded protein (GO:0006986)	49.21	2.54431E-10	33/135
cellular response to unfolded protein (GO:0034620)	48.68	2.54431E-10	27/86
response to topologically incorrect protein (GO:0035966)	47.27	6.88308E-10	33/143
cellular response to topologically incorrect protein (GO:0035967)	46.65	6.88308E-10	27/92
protein N-linked glycosylation via asparagine (GO:0018279)	34.18	1.75157E-07	24/96
peptidyl-asparagine modification (GO:0018196)	34.03	1.86284E-07	24/97
gene expression (GO:0010467)	33.91	4.40708E-07	70/672

Cellular Component	Combined Score	FDR	Overlap
endoplasmic reticulum membrane (GO:0005789)	30.02	2.01305E-06	53/449
nucleoplasm (GO:0005654)	28.28	3.29534E-06	92/1051
integral component of endoplasmic reticulum membrane (GO:0030176)	12.42	0.003300267	16/94
nucleolus (GO:0005730)	12.21	0.003300267	113/1653
cytosol (GO:0005829)	11.66	0.003300267	160/2529
endoplasmic reticulum-Golgi intermediate compartment (GO:0005793)	9.24	0.014361872	10/47
integral component of organelle membrane (GO:0031301)	6.51	0.049290428	22/211
anchoring junction (GO:0070161)	6.34	0.057276314	35/419
adherens junction (GO:0005912)	6.27	0.057276314	34/405
late endosome (GO:0005770)	5.94	0.056552892	14/107

Molecular Function	Combined Score	FDR	Overlap
phosphate transmembrane transporter activity (GO:1901677)	6.21	0.119107898	6/20
nucleotide transmembrane transporter activity (GO:0015215)	5.85	0.119107898	5/15
intramolecular oxidoreductase activity, transposing S-S bonds (GO:0016864)	5.75	0.119107898	6/22
protein disulfide isomerase activity (GO:0003756)	5.67	0.119107898	6/22
low-density lipoprotein particle receptor binding (GO:0050750)	5.65	0.119107898	5/13
nucleotide-sugar transmembrane transporter activity (GO:0005338)	5.60	0.110256823	5/8
organophosphate ester transmembrane transporter activity (GO:0015605)	5.45	0.130610086	5/16
isomerase activity (GO:0016853)	5.15	0.110256823	19/159
unfolded protein binding (GO:0051082)	4.73	0.119107898	13/101
lipoprotein particle receptor binding (GO:0070325)	4.72	0.160729311	5/18

b

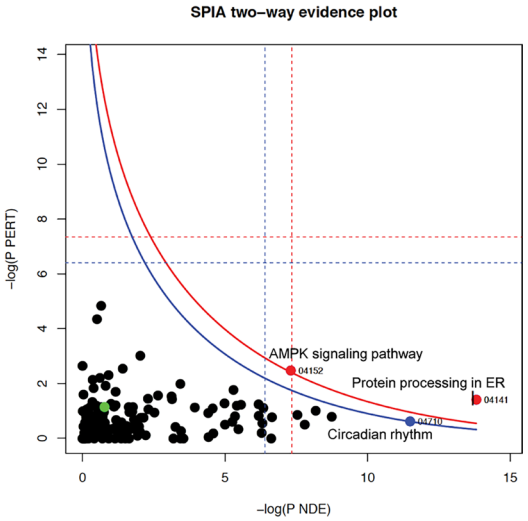

Extended Data Fig. 2 | Pathway analysis for hepatic significant genes. (**a**) Gene ontology analysis for down- and up-regulated HFD-responsive genes. (**b**) Signaling pathway impact analysis (SPIA) for HFD-responsive genes was conducted as described[80]. Pathways respectively on the right-hand side of the red and blue curves are significant after Bonferroni correction of the global p-values (pG) obtained by combining the pPERT and pNDE using the normal inversion method, and significant after a FDR correction of pG using the Benjamini – Yekutieli method. Significant KEGG pathways: 04141, Protein processing in the endoplasmic reticulum; 04710, Circadian rhythm; 04152, AMPK signaling pathway. Source data are provided.

https://doi.org/10.1038/s42255-025-01413-8

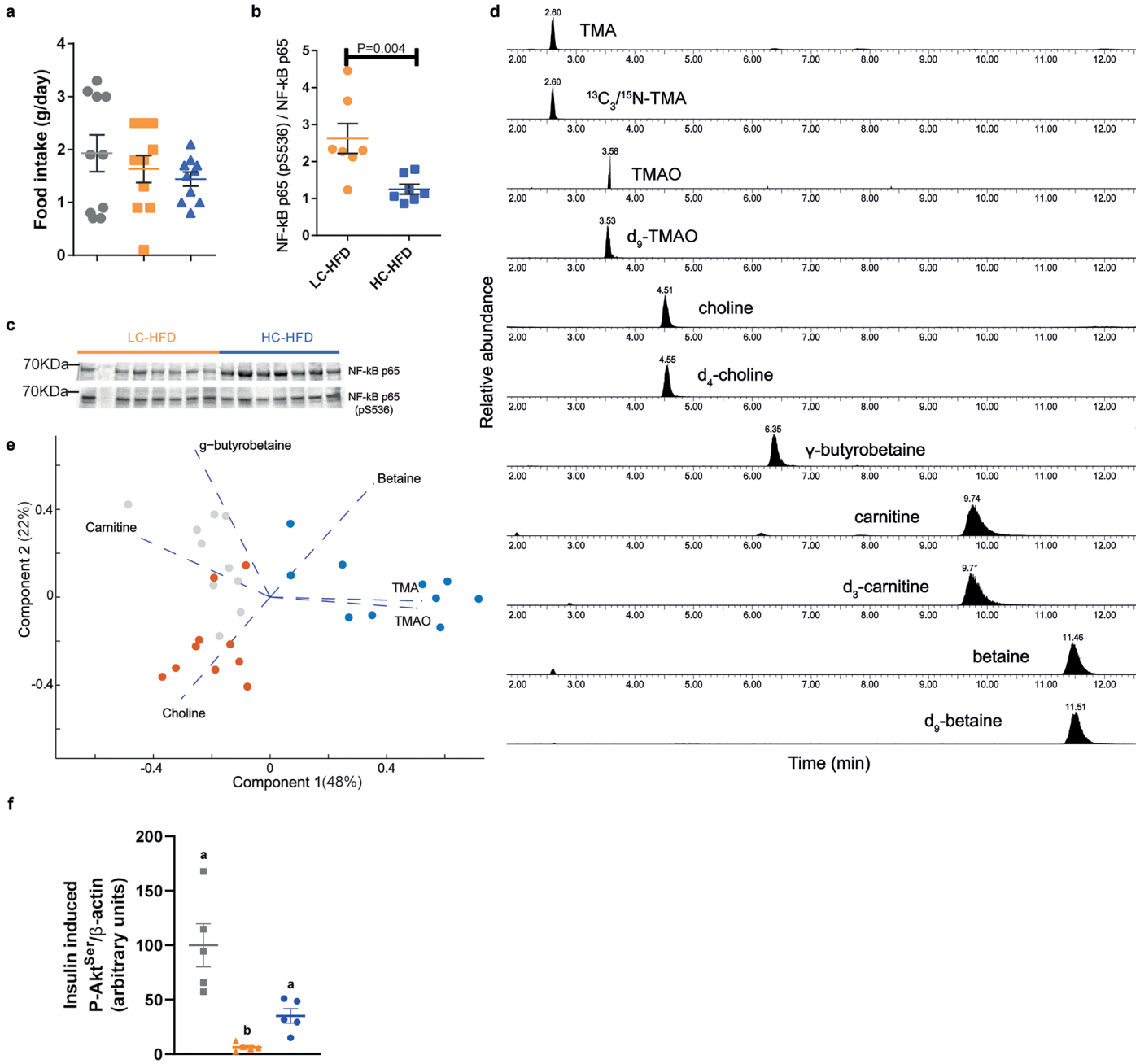

Extended Data Fig. 3 | Choline supplementation corrects HFD adverse effects and associated methylamine measurements. (**a**) Food intake measured on the three tested diets (CHD, LC-HFD and HC-HFD), with each dot representing a single mouse. (**b**, **c**) Western blot analysis of liver NF-kB phosphorylation state between LC-HFD and HC-HFD (N = 7 per diet). In (**b**) each dot represents densitometric analysis of NF-κB^{Ser536} phosphorylation in liver extracts of a single mouse from the blot in (**c**). (**d**) Plasma sample chromatogram for the simultaneous detection of TMA, TMAO, choline, γ-butyrobetaine, carnitine, betaine and their isotopically labelled analogues. (**e**) Principal Component Analysis Biplot of plasma methylamine quantifications by UPLC/MS-MS from mice fed CHD, LC-HFD and HC-HFD, each component's explained variance is shown in parenthesis. Data are means ± s.e.m. Two-sided Mann-Whitney test (*$P < 0.05$ vs control). (**f**) Densitometric analyses of western blots in Fig. 2g using β-actin to correct Akt levels prior to pAkt normalization. Each data point represents pAkt^{Ser473}/β-actin ratio in liver extracts of a single mouse. Data are means ± s.e.m. One-way ANOVA followed by Tukey's *post hoc* tests (superscript letters for factor levels $P < 0.05$) on log-transformed data. Source data are provided.

https://doi.org/10.1038/s42255-025-01413-8

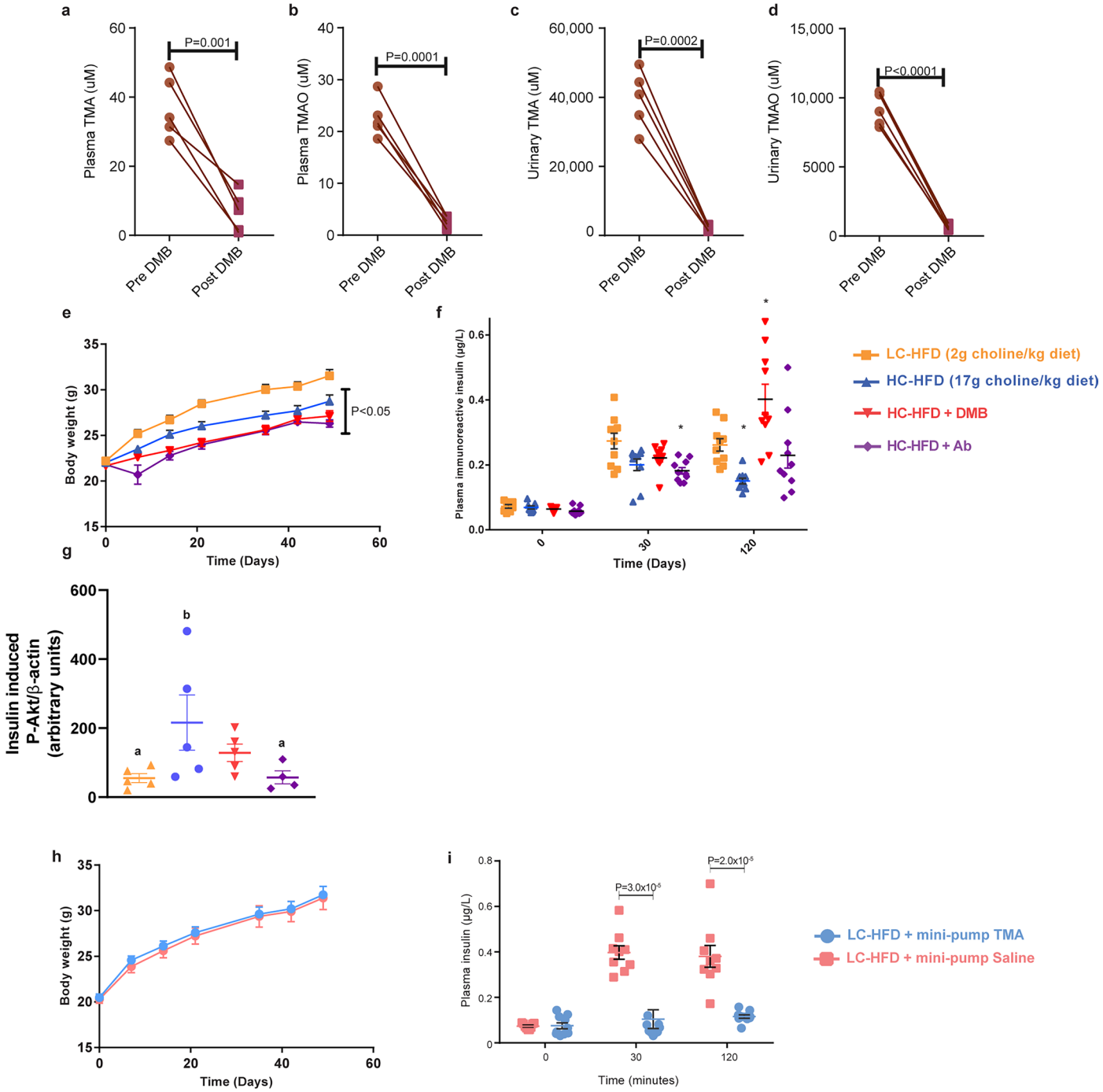

Extended Data Fig. 4 | Modulation of TMA production and effects. (**a**–**d**) Confirmation of blockage of production of TMA (**a**, **c**) and TMAO (**b**, **d**) by 1% DMB measured in plasma (**a**, **b**) and urine (**c**, **d**). Each line represents TMA or TMAO levels trajectories pre (circles) or post (squares) DMB treatment in a single mouse (**e**) Body weight monitoring during the whole experiment of mice fed a LC-HFD and a HC-HFD supplemented or not with DMB or treated with antibiotics. (**f**) Plasma insulin concentration during GTT at 0, 30 and 120 min post glucose injection. (**g**) Densitometric analyses of western blots in Fig. 3d using β-actin to correct Akt levels prior to pAkt normalization. One-way ANOVA followed by Tukey's *post hoc* tests (superscript letters for factor levels $P < 0.05$) on log-transformed data. For (e-g) each dot represents data from a single mouse. (**h**) Body weight monitoring during the whole experiment of mice fed a LC-HFD and chronically treated with TMA (N = 10; light blue) or saline (N = 10; light red). (**i**) Plasma insulin concentration during GTT at 0, 30 and 120 min post glucose injection. Each data point represents data from a single mouse. Data are means ± s.e.m. Two-sided Mann-Whitney test (*$P < 0.05$ vs LC-HFD control). Source data are provided.

https://doi.org/10.1038/s42255-025-01413-8

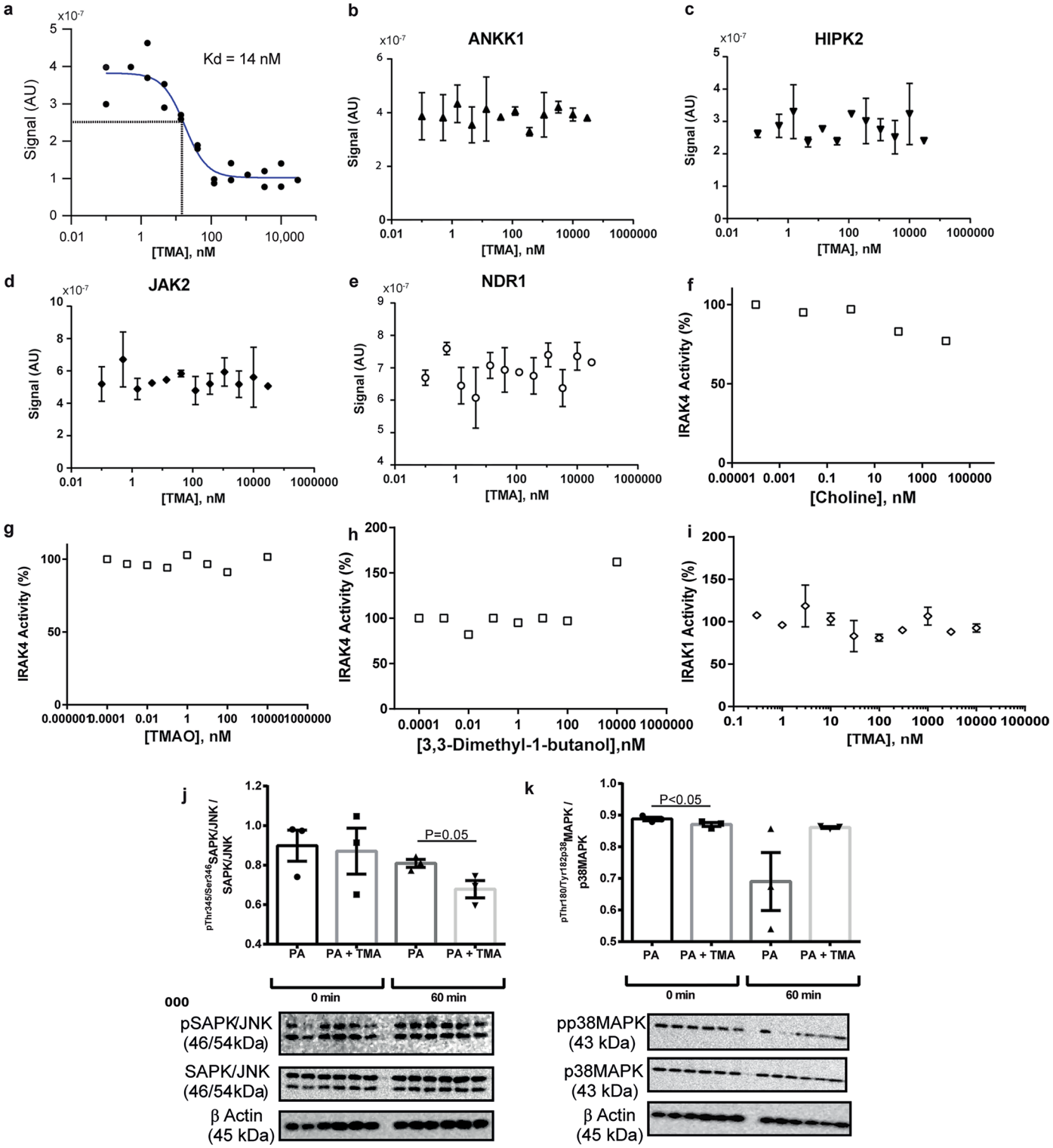

Extended Data Fig. 5 | TMA does not bind with kinases ANKK1, HIPK2, JAK2, and NDR1 identified as candidates in the kinome screen, but makes significant contact with IRAK4. (**a**) Confirmation of a physical interaction between TMA and IRAK4 using TMA at concentrations ranging from 0.1 nM to 100 µM, resulting in a dissociation constant (K_d) of 14 nM. (**b**–**e**) Physical interaction test between TMA and the four hits identified using a kinome screen, using TMA concentrations ranging from 0.1 nM to 100 µM for (**b**) ANKK1, (**c**) HIPK2, (**d**) JAK2 and (**e**) NDR1. For (b-e) N = 2 biological repeats. IRAK4 kinase activity is not significantly inhibited by choline (**f**), TMAO (**g**) or DMB (**h**), while TMA does not have any inhibitory effect on IRAK-1 kinase activity (average of N = 2 biological repeats) (**i**). (**j**, **k**) Phosphorylation for $^{pThr183/Tyr185}$SAPK/JNK/SAPK/JNK (**j**) and $^{pThr180/Tyr182}$p38MAPK/p38MAPK (**k**) densitometric ratios, represented by each dot. Data are means ± s.e.m. One-way ANOVA followed by Tukey's *post hoc* tests (superscript letters for factor levels $P < 0.05$) on log-transformed data. Source data are provided.

https://doi.org/10.1038/s42255-025-01413-8

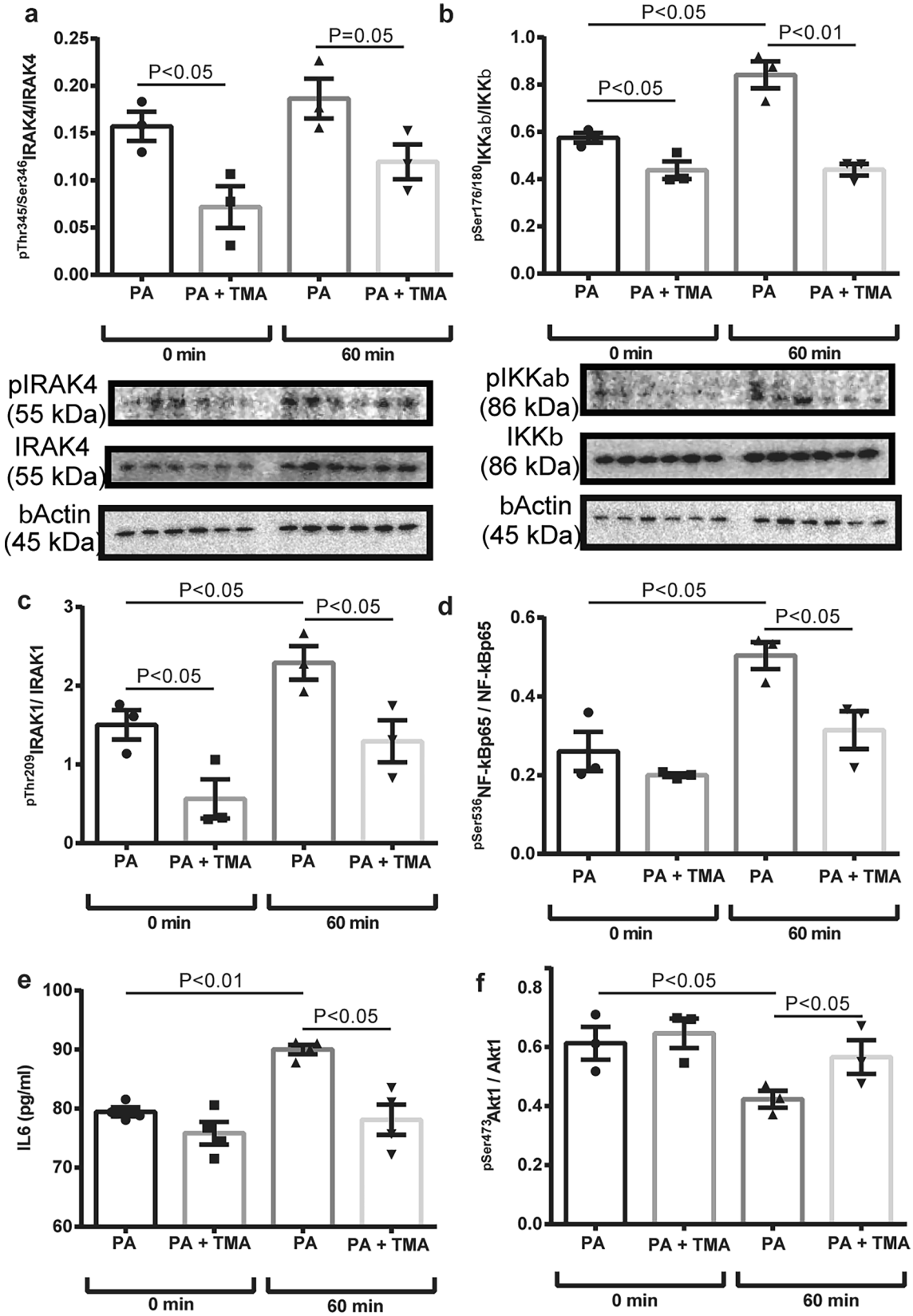

Extended Data Fig. 6 | See next page for caption.

https://doi.org/10.1038/s42255-025-01413-8

Extended Data Fig. 6 | TMA inhibits IRAK4 and suppresses TLR4-mediated pro-inflammatory response in primary human hepatocytes. (**a**–**d**) Effect of palmitate (PA; 200 µM) administration and TMA pre-treatment (0.1 mM, 30 min) in primary human hepatocytes at 0 and 60 min on $^{pThr345/Ser346}$IRAK4/IRAK4 (**a**), $^{pSer176/180}$IKKαβ/IKKβ (**b**), ^{pThr209}IRAK1/IRAK1 (**c**), ^{pSer536}NF-κBp65/NF-κBp65 (**d**) ratios. For (a-b) each dot represents densitometric ratios of relative phosphorylation levels from hepatocyte lysates from 3 independent biological repeats, treated as indicated. $^{*}p < 0.05$ and $^{**}p < 0.01$ *vs* 0 min; $^{\dagger}p < 0.05$ and $^{\dagger\dagger}p < 0.01$ *vs* vehicle; $^{b}p = 0.07$ *vs* vehicle. Effect of PA (200 µM) administration (4 h) with and without TMA pre-treatment (0.1 mM, 30 min) on IL6 accumulation in hepatocyte media (**e**) and on ^{pSer473}Akt1/Akt1 after insulin stimuli (100 nM, 10 min) (**f**). Each dot represents an independent biological repeat. $^{*}p < 0.05$ and $^{**}p < 0.01$ *vs* control-vehicle; $^{\dagger}p < 0.05$ *vs* control-PA. For (a-f) data are means ± s.e.m and statistical significance was determined by one-way ANOVA followed by Tukey's *post hoc* tests on log-transformed data. Source data are provided.

https://doi.org/10.1038/s42255-025-01413-8

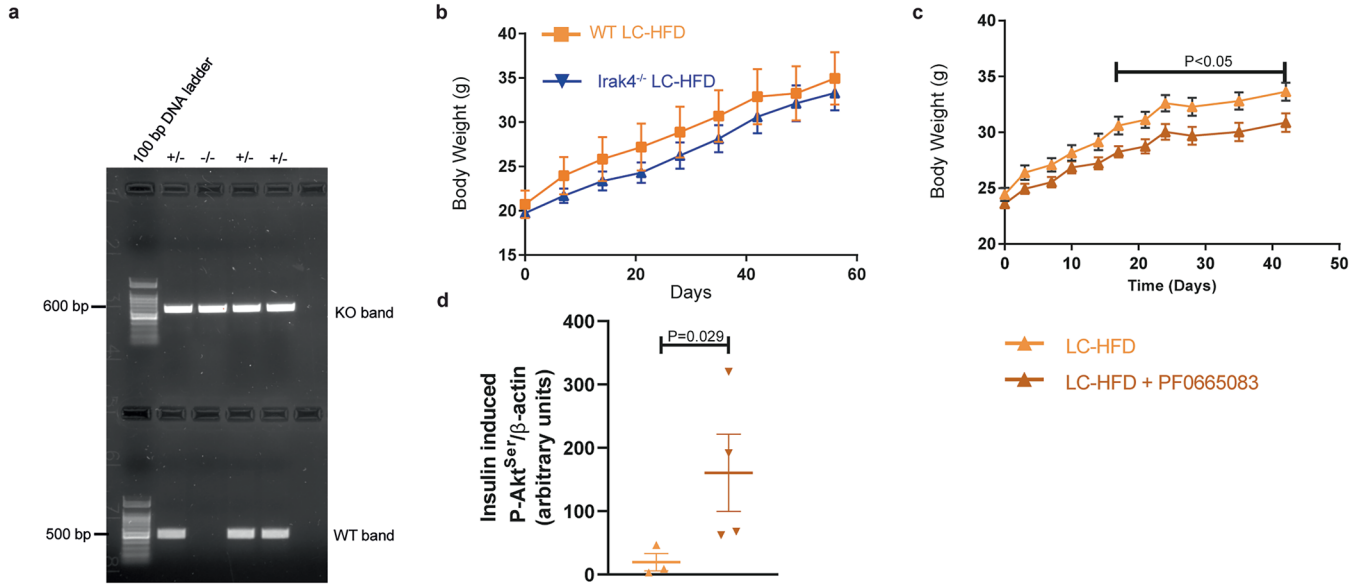

Extended Data Fig. 7 | IRAK4 knock-out does not affect body weight while chronic treatment with PF06650833 reduces it in mice fed a low-choline HFD. (**a**) Indicative agarose gel of PCR products from +/-irak4 and -/-irak4 mice. (**b**, **c**) Body weight monitoring during the whole experiment of *Irak4*$^{-/-}$ mice (N = 9) or wild-type controls (N = 9) (**b**) or PF06650833-treated (N = 9-13) or vehicle-treated (N = 6) mice (**c**) fed a LC-HFD. (**d**) Densitometric analyses of western blots in Fig. 5m using β-actin to correct Akt levels prior to pAkt normalization. Each data point represents pAKT^{Ser473}/β-actin ratio from a single mouse liver. Data are means ± s.e.m. double-sided unpaired Student's *t* test (*$P < 0.05$) on log-transformed data. Source data are provided.

nature portfolio

Corresponding author(s): Prof. ME Dumas

Last updated by author(s): 2025/09/15

Reporting Summary

Nature Portfolio wishes to improve the reproducibility of the work that we publish. This form provides structure for consistency and transparency in reporting. For further information on Nature Portfolio policies, see our Editorial Policies and the Editorial Policy Checklist.

Statistics

For all statistical analyses, confirm that the following items are present in the figure legend, table legend, main text, or Methods section.

n/a	Confirmed	
☐	☒	The exact sample size (*n*) for each experimental group/condition, given as a discrete number and unit of measurement
☐	☒	A statement on whether measurements were taken from distinct samples or whether the same sample was measured repeatedly
☐	☒	The statistical test(s) used AND whether they are one- or two-sided *Only common tests should be described solely by name; describe more complex techniques in the Methods section.*
☐	☒	A description of all covariates tested
☐	☒	A description of any assumptions or corrections, such as tests of normality and adjustment for multiple comparisons
☐	☒	A full description of the statistical parameters including central tendency (e.g. means) or other basic estimates (e.g. regression coefficient) AND variation (e.g. standard deviation) or associated estimates of uncertainty (e.g. confidence intervals)
☐	☒	For null hypothesis testing, the test statistic (e.g. *F*, *t*, *r*) with confidence intervals, effect sizes, degrees of freedom and *P* value noted *Give P values as exact values whenever suitable.*
☒	☐	For Bayesian analysis, information on the choice of priors and Markov chain Monte Carlo settings
☒	☐	For hierarchical and complex designs, identification of the appropriate level for tests and full reporting of outcomes
☐	☒	Estimates of effect sizes (e.g. Cohen's *d*, Pearson's *r*), indicating how they were calculated

Our web collection on statistics for biologists contains articles on many of the points above.

Software and code

Policy information about availability of computer code

Data collection	MassLynxTM (Waters corporation; Version 4.2) software was used for UPLC-MS/MS data acquisition and analysis. 1H-NMR absolute quantifications were derived using the "In Vitro Diagnostics for research" (IVDr) algorithm (Bruker; v1.1). Image analyses of western blot films and immunohistochemistry slides was conducted with ImageJ (NIH; v1.46r)
Data analysis	Analysis was conducted using the R (v4.03) statistical language as described in the Methods. No custom software was used in this project.

For manuscripts utilizing custom algorithms or software that are central to the research but not yet described in published literature, software must be made available to editors and reviewers. We strongly encourage code deposition in a community repository (e.g. GitHub). See the Nature Portfolio guidelines for submitting code & software for further information.

Data

Policy information about availability of data

All manuscripts must include a data availability statement. This statement should provide the following information, where applicable:

- Accession codes, unique identifiers, or web links for publicly available datasets
- A description of any restrictions on data availability
- For clinical datasets or third party data, please ensure that the statement adheres to our policy

Microarray data are deposited in ArrayExpress under accession number E-MEXP-1755. 1H-NMR mouse metabolomics have been uploaded to Metabolights with

accession number MTBLS12989 (https://www.ebi.ac.uk/metabolights/MTBLS12989). The UPLC-MS/MS spectra for Isotopically quantified methylamines have been deposited to Metabolights with accession number MTBLS12975 (https://www.ebi.ac.uk/metabolights/MTBLS12975).

Research involving human participants, their data, or biological material

Policy information about studies with human participants or human data. See also policy information about sex, gender (identity/presentation), and sexual orientation and race, ethnicity and racism.

Reporting on sex and gender	PBMCs were isolated from 25 - 32 year old female healthy (by self-declaration) volunteers.
Reporting on race, ethnicity, or other socially relevant groupings	Please see below
Population characteristics	Subjects were used only for PBMCs isolation. Since PBMCs from the same participant served as the control (no LPS and/or TMA challenge) and the treatment groups in each independent biological repeat of the experiments in Figure 4 no covariate adjustment was necessary.
Recruitment	Members of the Department of Metabolism Digestion and Reproduction, Imperial (N=4) volunteered to provide blood after a request circulated within the Department. Volunteers received no financial compensation.
Ethics oversight	Imperial College Research Ethics Committee (19IC5372).

Note that full information on the approval of the study protocol must also be provided in the manuscript.

Field-specific reporting

Please select the one below that is the best fit for your research. If you are not sure, read the appropriate sections before making your selection.

☒ Life sciences ☐ Behavioural & social sciences ☐ Ecological, evolutionary & environmental sciences

For a reference copy of the document with all sections, see nature.com/documents/nr-reporting-summary-flat.pdf

Life sciences study design

All studies must disclose on these points even when the disclosure is negative.

Sample size	No sample-size calculation was performed. Sample sizes for the animal experiments were based on previous extensive knowledge of the authors with similar experimental designs to decipher the impact of microbial metabolites on the host (e.g.: please see our study for the metabolite hippurate Brial, F. et al. Gut 70, 2105–2114 (2021)).
Data exclusions	No data where excluded from the animal studies. In the PBMC experiments (Figure 4) one data point was excluded (with high baseline IL6 and TNFa) after the volunteer reported subsequently to the experiment that had received COVID vaccination 3 days prior blood collection.
Replication	To replicate the main finding of our study suggesting a direct inhibitory effect of TMA on IRAK4 kinase activity resulting in alleviated metabolic inflammation and Insulin Resistance (IR) in the host we used multiple distinct but mutually supporting experimental approaches. Specifically, mice were treated with high-choline high-fat diet (HC-HFD which would increase TMA through the microbiome) with or without antibiotics or DMB (an inhibitor of choline conversion to TMA by the microbiome). The beneficial effect of HC-HFD on host glucose handling and IR were abolished by antibiotics or DMB and were emulated by TMA challenge in separate animal experiments. IRAK4 knockout in mice or pharmacological inhibition of its activity by a specific inhibitor also had a beneficial effect on host IR and glucose handling similarly to TMA treament (which would suppress IRAK4 kinase activity). TMA was shown to bind to purified IRAK4 in a pan-kinase screen and to inhibit dose-dependently purified IRAK4 kinase activity. Finally, TMA suppressed cytokine release by human PBMCs stimulated by LPS and rescued an LPS-challenged mouse septic shock model; both processes dependent on IRAK4 kinase activity. Collectively, through a battery of independent experiments ranging from purified proteins to cells and animals we extensively replicated the main thrust of our study i.e: TMA improves host metabolic health by inhibiting IRAK4 kinase activity. For the cellular studies there were at least 3 independent biological repeats. All animal studies were conducted once with 6-10 animals per experimental group. All animal experimental groups were treated concurrently.
Randomization	In the animal study, mice were randomly assigned to experimental groups.
Blinding	Where possible experimentalists were blinded. This is clearly stated in the Methods for each relevant experiment.

Reporting for specific materials, systems and methods

We require information from authors about some types of materials, experimental systems and methods used in many studies. Here, indicate whether each material, system or method listed is relevant to your study. If you are not sure if a list item applies to your research, read the appropriate section before selecting a response.

Materials & experimental systems

n/a	Involved in the study
☐	☒ Antibodies
☐	☒ Eukaryotic cell lines
☒	☐ Palaeontology and archaeology
☐	☒ Animals and other organisms
☒	☐ Clinical data
☒	☐ Dual use research of concern
☒	☐ Plants

Methods

n/a	Involved in the study
☒	☐ ChIP-seq
☒	☐ Flow cytometry
☒	☐ MRI-based neuroimaging

Antibodies

Antibodies used

Membranes were immunoblotted with antibodies against the following proteins: pThr345/Ser346IRAK4 (#11927), IRAK4 (#4363), pSer176/180IKKαβ (#2694), IKKβ (#8943), pThr183/Tyr185SAPK/JNK (4668), SAPK/JNK (#9258), pThr180/Tyr182p38MAPK (#9215), p38MAPK (#9212) p-Akt Ser473 (1:1,000; #4060), Total Akt (1:1000 ,#9272S), Total NF- κB p65 (1:3000, #8242), all purchased from Cell Signaling Technology, Inc (CST, MA, USA); β-actin (sc-47778, Santa Cruz Biotechnology, CA, USA) and p-NF-κB (1:3000, #ab86299) from AbCam.

Validation

All the antibodies were sourced commercially and extensively reported in the literature and validated by the vendors. Therefore, no specific validation was performed.

Eukaryotic cell lines

Policy information about cell lines and Sex and Gender in Research

Cell line source(s)

PBMCs were isolated from female volunteers (25-32 years old).

Primary human hepatocytes were commercially sourced (Innoprot, Bizkaia, Spain)

Authentication

PBMCs responded to LPS challenge in an IRAK4-dependent manner as extensively reported in the literature. Therefore no other specific validation was carried out.

Primary human hepatocytes were commercially sourced, had the expected morphology and responded to palmitate similarly to previous reports in the literature. We therefore, did not further validate them.

Mycoplasma contamination

PBMCs were isolated from human volunteers and used within one hour of isolation. Therefore, no mycoplasma testing was performed.

Primary human hepatocytes (HHs) were commercially sourced and tested by the vendor for mycoplasma. Since HHs were used in experiments within 24h of plating no mycoplasma test was performed.

Commonly misidentified lines
(See ICLAC register)

Not applicable

Animals and other research organisms

Policy information about studies involving animals; ARRIVE guidelines recommended for reporting animal research, and Sex and Gender in Research

Laboratory animals

Five to six week-old C57BL/6J male mice at the start of the experiment were used in this study.

Wild animals

Not applicable

Reporting on sex

Only male mice were used in our study.

Field-collected samples

Not applicable

Ethics oversight

All experimental procedures involving mice were carried out in accordance with U.K. Home Office, Canadian Council on Animal Care, the ethics committee of the French Research Ministry (authorization number 00486.01), Belgian Law of May 29, 2013 regarding the protection of laboratory animals (agreement number LA1230314) and local guidelines on animal welfare and license conditions and the University of Oxford, University of Ottawa, Université Pierre et Marie Curie and Université catholique de Louvain guidelines on animal welfare. For the septic shock study the animal experiment protocol was approved by local and national committees in charge (Tor Vergata University Institutional Animal Care and Use Committee and Ministry of Health, license no. 265/2019-PR).

Note that full information on the approval of the study protocol must also be provided in the manuscript.

Plants

Seed stocks	Not applicable
Novel plant genotypes	Not applicable
Authentication	Not applicable